



Fretting-fatigue of shrink fit lug-bush assemblies: Interference-fit effect

M. Le Falher, Siegfried Fouvry, Pierre Arnaud, Vincent Maurel, N. Antoni, R.
Billardon

► To cite this version:

M. Le Falher, Siegfried Fouvry, Pierre Arnaud, Vincent Maurel, N. Antoni, et al.. Fretting-fatigue of shrink fit lug-bush assemblies: Interference-fit effect. Tribology International, 2023, 186, pp.108581. 10.1016/j.triboint.2023.108581 . hal-04220410

HAL Id: hal-04220410

<https://hal.science/hal-04220410>

Submitted on 10 Oct 2023

HAL is a multi-disciplinary open access archive for the deposit and dissemination of scientific research documents, whether they are published or not. The documents may come from teaching and research institutions in France or abroad, or from public or private research centers.

L'archive ouverte pluridisciplinaire **HAL**, est destinée au dépôt et à la diffusion de documents scientifiques de niveau recherche, publiés ou non, émanant des établissements d'enseignement et de recherche français ou étrangers, des laboratoires publics ou privés.

M. Le Falher, S. Fouvry, P. Arnaud, V. Maurel, N. Antoni, R. Billardon, Fretting-fatigue of shrink fit lug-bush assemblies: Interference-fit effect, Tribology International 186 (2023) 108581 (<https://doi.org/10.1016/j.triboint.2023.108581>)

FRETTING-FATIGUE OF SHRINK FIT LUG-BUSH ASSEMBLIES: INTERFERENCE-FIT EFFECT

M. LE FALHER(1,2,3)*, S. FOUVRY(1)*, P. ARNAUD(2), V. MAUREL(2), N. ANTONI(4), R. BILLARDON(3)

(1) Ecole Centrale de Lyon, Laboratoire de Tribologie et Dynamique des Systèmes (LTDS), Ecully, France

(2) Centre des Matériaux, Mines Paris – ParisTech, Evry, France

(3) Safran Transmission Systems, Colombes, France

(4) Safran Landing Systems, Vélizy, France

* Corresponding authors email addresses : melody.le-falher@ec-lyon.fr, siegfried.fouvry@ec-lyon.fr

Abstract:

The fretting-fatigue behaviour of shrink fit lug-bush assemblies is investigated. In this paper, experimental fatigue tests are carried out on lug-bush specimens with three different levels of interference fit. It is observed that the relative movements of fretting induce tribo-oxidation phenomena at the shrink-fit interface and that the crack initiation sites correspond well to the oxides formation spots. The increase in the fatigue life with interference fit is consistent with stress analysis considering the SWT multiaxial fatigue criterion, but the predicted fatigue life is not conservative relative to material reference data. In order to account for fretting surface damage, different approaches are investigated considering homogeneous and heterogeneous distributions of the coefficient of friction.

Keywords:

Fretting; Fatigue; Lug-bush; Interference-fit; Ti-6Al-4V

Nomenclature:

P [N]: normal force

Q^* [N]: tangential force amplitude

δ^* [μm]: displacement amplitude

σ_{nom} [MPa]: nominal stress

N_c : number of cycles

IT [μm]: interference fit (between lug and bush)

C [μm]: clearance fit (between shaft and bush)

DIT [μm]: degree of interference

δ [μm]: relative sliding

Δ_s [μm]: relative sliding amplitude per cycle

φ [m]/ mm^2 : surface density of the dissipated energy per cycle

$\sigma_{SWT_{max}}$ [MPa]: maximum SWT equivalent stress at the lug bore

A_{net} [mm^2]: lug net section

FWS: Fretting Wear Spot

1. Introduction:

Lug assembly is a widely used type of joint in aeronautical industry [1]. The joint is composed of parts called fork and lug, the load transmission being ensured by a shaft (Figure 1).

Under loading, lug holes act as geometric discontinuities inducing stress concentrations. Peak stress at the lug bore depends on several geometric parameters (bore to lug width ratio, pin-lug allowance...) and have been summarised for various works into charts for design optimization [1][2][3][4]. Under fatigue loading, additional surface damage is observed due to the relative sliding between the parts, called fretting [5][6].

An oversized bush is sometimes inserted into the lug bore by shrink or press fitting. Several studies have shown an increase in the lug fatigue life with increasing interference-fit for different lug-bush materials (Aluminium 7075 [7][8][9][10], Inconel 718 [11] and Ti-6Al-4V [12]).

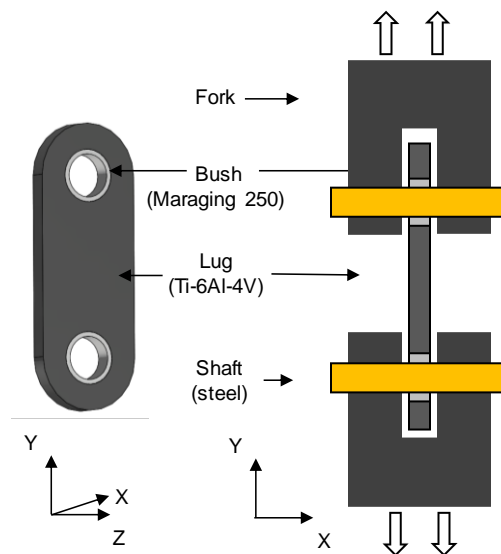


Figure 1: Illustration of lug-bush assembly

Historically, the beneficial effect of this interference fit has been attributed to two phenomena: the stress distribution effect and the fretting effect [7][10]. On the one hand, the interference fit modifies the stress distribution because it induces a pre-stressed state [7]. Finite element modelling has confirmed, for bolted joints and lug-bush joints, that interference fit reduces local stress amplitude, increasing at the same time fatigue life [10][13]. On the other hand, the increase of fatigue life with the interference fit has been attributed to a reduction of fretting damage [7]. In fact, under cyclic loading, the lug-bush parts deform causing relative sliding at the lug-bush interface and sometimes a separation of the contact. The combination of fretting and fatigue loading usually results in wear and early crack initiation; the crack propagation being driven by bulk fatigue loading. In this case, the reduction in relative sliding by increasing the interference fit was expected to reduce the relative sliding amplitude and then, the fretting damage at the lug-bush interface.

Several studies have outlined fretting-wear damage at the shrink-fit interface but in-depth analysis of surface damage is scarcely developed. Fisher and Winkworth [7] noted superficial wear damage on the bushes while Wardlaw and al. [12] observed “fretting” marks at crack initiation sites on their lug specimens. Buch [8] suggested a possible effect of surface oxidation and third body on crack initiation for aluminium alloy lugs. Ozen [14] showed oxide formation at the lug-bush contact of TA6V-steel parts. The underlying idea behind the cited publications is that wear phenomena may favour crack initiation.

The lug-bush contact belongs to the class of conforming contacts [15], meaning the contact parts fit into each other with a high degree of geometrical conformity. Conforming contacts are characterised by a relatively large contact area, low contact pressure and low stress concentration compared to classical non-conforming contacts (cylinder-on-flat, sphere-on-flat, crossed-cylinder contacts, etc.). Non-conforming fretting contact results are generally hard to transpose to conforming ones. For the latter, contact pressure, peak stresses and stress gradients are lower [6] and wear is shallower due to the entrapment of debris particles within the large contact area [16]. However, a large proportion of industrial contacts is conformal [17]. Several cases of premature failure of interference fit connecting rods, for a large number of cycles, have been explained by the formation of adhesive spots [18][19]. It has been shown that the contact between conforming parts with a contact pressure as low as 50 MPa and a small relative sliding ($< 20 \mu\text{m}$) can lead to adhesive spots driving crack initiation [20].

Most of the lug-bush fatigue life analyses have focused on the stress distribution, excluding the effect of wear [10][11][12][21]. The effect of surface damage on crack initiation remains a challenging issue.

Empirical strategies exist which consider fretting damage in conforming contacts. Ruiz [22] established a surface damage criterion (Γ_{Ruiz}) expressed as the product of the maximum opening stress, the shear stress and the sliding amplitude. This criterion, which was originally developed to study fretting problems in dovetail joint, arouses some interest in the study of connecting rods and bolted joints [23][24] as well as rolling contacts [25]. However, this criterion remains very empirical and it is not possible to correlate Γ_{Ruiz} values with material properties. Combinations of fatigue criteria and tribological parameters have also been developed such as the SWT modified parameter [26][27].

The objective of this work is to study the fretting-fatigue behaviour of conforming contacts, specifically the behaviour of lug-bush shrink-fit assemblies for different levels of interference fit. Several aspects are analysed:

- How does lug-bush interference fit affect the fatigue life of the assembly?

- What type of surface degradation is observed at the lug-bush interface and how does it affect crack initiation?

To answer these questions, experimental tests, detailed surface analysis and numerical finite element analysis are combined. The results provide a basis for considering the integration of the effect of stress-strain and tribological loading for the lug-bush design method.

1. Experiments

2.1 Materials

The materials used for the lug-bush specimens are Maraging 250 steel (bush) and Ti-6Al-4V (lug). Maraging 250 steel is a high strength Fe-Ni martensitic steel, the chemical composition of which is given in Table 1. Ti-6Al-4V is an alpha titanium alloy with high specific strength and excellent corrosion resistance. Its chemical composition is given in Table 2. A 300 mm diameter bar is used with a solution treatment at 950 °C (water cooling) followed by aging for 2 hours at 700 °C (air cooling). The microstructure is bimodal consisting of approximately 35% hexagonal close-packed (hcp) primary alpha phase with the remainder consisting of acicular secondary α phase within the body center cubic (bcc) β phase (Figure 2). Large elongated (\sim several mm) ex-beta grains can be observed along the main direction of the bar. Uniaxial fatigue data from Hines [28] (bimodal microstructure with 35% primary alpha fraction phase) is used as reference (Figure 3).

The final properties of both alloys are detailed in Table 3. The fatigue limit of Ti-6Al-4V is 450 MPa at 10^7 cycles for a load ratio R of -1 according to Hines [28].

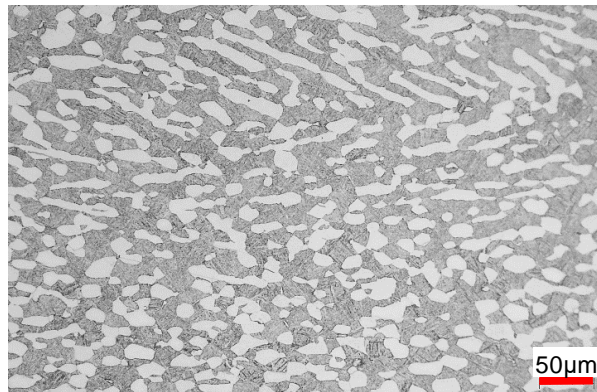


Figure 2: Bimodal microstructure of Ti-6Al-4V, after Kroll etching, showing primary alpha grains (white)

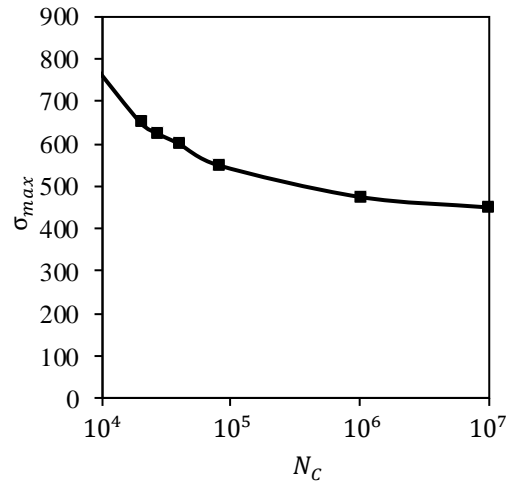


Figure 3: Fitting curve of the uniaxial fatigue life of Ti-6Al-4V (R = - 1) [28]

Ni	Co	Mo	Ti	C	Fe
18	8	5	0.5	0.03	Balance

Table 1: Chemical composition of Maraging 250 steel (weight %)

Al	V	Fe	O	C	N	Ti
6	4	<0.30	<0.02	<0.08	<0.07	Balance

Table 2: Chemical composition of Ti-6Al-4V (weight %)

Material	E (GPa)	ν	Vickers Hardness	Yield Strength (MPa)	Ultimate Strength, σ_u (MPa)	Fatigue limit 10^7 cycles (MPa)
Ti-6Al-4V	115	0.3	277 - 361	940 [28]	990 [28]	450 [28]
Maraging 250	184	0.3	490 - 589	1832	1893	

Table 3: Mechanical properties of Ti-6Al-4V and Maraging 250

2.2 Friction behaviour of Ti-6Al-4V – Maraging 250 interface

Friction behaviour of Ti-6Al-4V versus Maraging 250 was determined by a variable displacement test following the methodology of Fouvry *et al.* [29]. The test was carried out on a fretting test bench, with a Maraging 250 100 mm cylinder radius and a Ti-6Al-4V flat specimen. The normal over tangential force ratio at the partial to gross slip transition defines the transition friction coefficient μ_t [30]. Proudhon *et al.* [30] suggested that the transition friction coefficient is representative of the coefficient of friction in the partial slip contact.

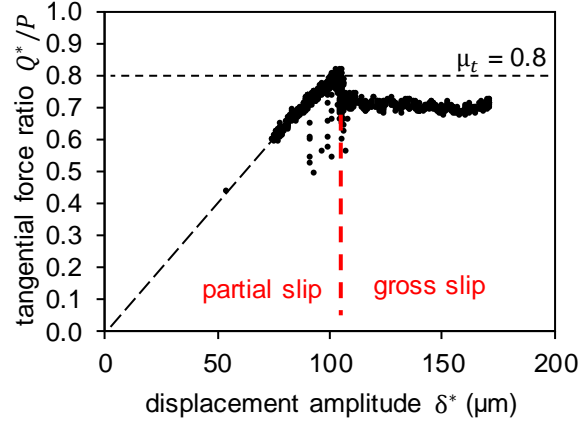


Figure 4: Friction coefficient at the sliding transition between partial and gross slip regimes of Ti-6Al-4V/Maraging 250 ($R_{cylinder} = 100$ mm, $p_{max} = 300$ MPa)

2.3 Specimen geometries

The lugs and bushes geometries are shown in Figure 5a. The bushes were cut to a larger diameter than the lugs bore. Three different bush diameters are used corresponding to three levels of interference fit (Table 4). The interference fit (IT) is defined as the difference between bush and lug hole diameter:

$$IT = \phi_{bush} - \phi_{lug} [\mu m] \quad (1)$$

and the degree of interference (DIT) as:

$$DIT = \frac{\phi_{bush} - \phi_{lug}}{\phi_{lug}} (\%). \quad (2)$$

Prior to assembly, the diameters of both the lugs bore and the bushes were systematically measured. Particular attention was paid to minimising the scatter of both lug-bush interference fits (± 2 μm) and bush-shaft clearance fits (± 3.5 μm). Prior to assembly, the clearance fits between the shaft and the bushes ($C = \phi_{bush} - \phi_{shaft}$ [μm]) were approximately 100 μm . Optical interferometry measurements showed that the roughness of the contact surfaces of the lugs and bushes was less than 0.25 μm .

The parts were cut to a width of 9 mm, and a chamfer was added to the inside diameter of the bushes. The bushes were shrunk into the lug holes after cleaning of the surfaces with acetone. The assemblies were then cut to a width of 8 mm to remove the chamfers.

After assembly, mechanical equilibrium at room temperature induces a positive contact pressure at the lug-bush interface which can be defined analytically by Lamé's equation or by numerical simulation (Table 4).

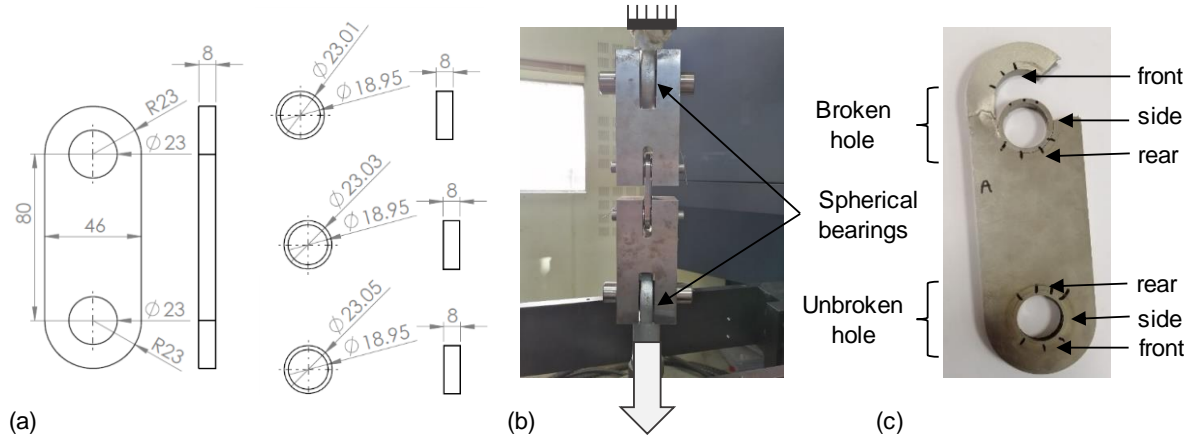


Figure 5: (a) Lug and bush geometries (in millimeters), (b) test bench, (c) description of specimen main zones

IT (μm)	DIT (%)	p (MPa) Lame's equation	p (MPa) numerical simulation
10	0.04	10.8	10.0 ± 0.3
30	0.13	32.5	30.3 ± 0.4
50	0.22	54.2	50.6 ± 0.6

Table 4: Interference fit levels and the associated contact pressures using Lame's equation and numerical simulations (see 4.1 numerical model)

2.4 Test conditions

Tests were conducted on a 150 kN MTS servo-hydraulic test system. The specimens were hold by steel fork systems with 18.85 mm diameter pins (Figure 5b). The pin-bush allowance of assembled specimens ranges from 60 and 100 μm according to the lug-bush interference fit. The forks were connected to a hydraulic actuator by spherical bearings on each side in order to accommodate potential small misalignments. The good alignment of the test bench was confirmed by the evenly distributed cracking sites among the four potential failure zones of the specimens (left and right sides of the top and bottom holes). The loading signal was a 15 Hz and 30 Hz sinusoidal wave, with an R-ratio of 0.1. The nominal stress is defined as the ratio of the maximum applied force to the net area of the lug ($A_{net} = 23 \times 8 \text{ mm}^2$) of lug.

Fatigue tests were conducted up to failure of the assemblies or stopped if unbroken after 10^7 cycles. The bushes and the lugs were marked prior to testing and no rotation of the bushes was observed. Both broken and unbroken sides of the specimens were examined. The description of the different parts of a tested specimen and the locations on the lug-bush interface (rear, side, front) are given in Figure 5c. In order to simplify the analysis and taking advantage of symmetries, cracks locations are systematically represented on the right side of the top hole. Unbroken sides of the lugs have been sawn to separate lug-bush parts without damaging the contact surfaces. To observe the lug-bush interface, some specimens were cold mounted prior to sawing.

2. Experimental results

3.1 Fatigue endurance and fretting scar expertise

The experimental fatigue life of the specimens was considered to be the total fatigue life (crack initiation and propagation). The results of the fatigue tests are shown in the nominal stress vs. number of cycles to failure $S-N_c$ plot (Figure 6). An increase in fatigue life with the degree of interference fit is observed, in agreement with literature results [10].

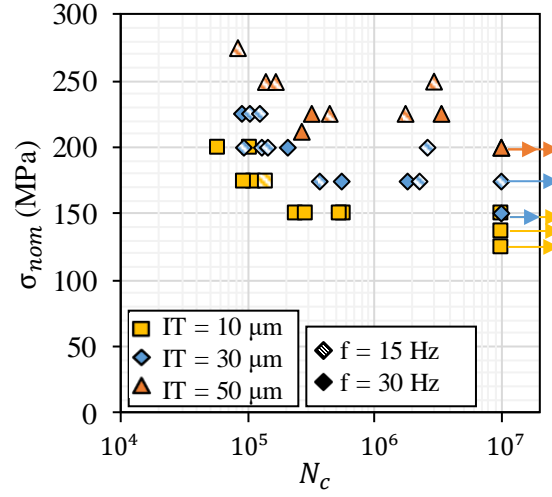


Figure 6: $S-N_c$ graph of the tested specimens for different levels of interference fit.

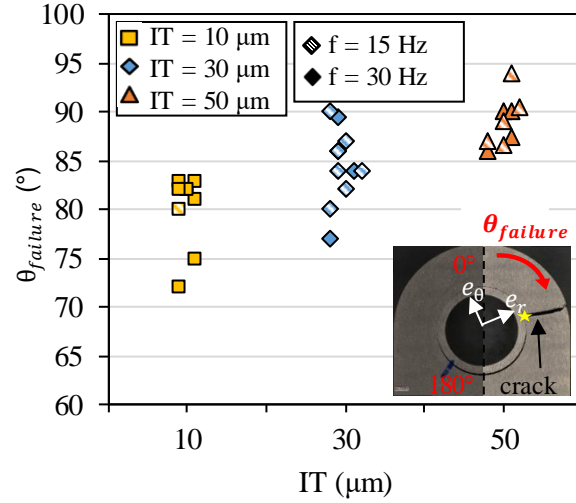


Figure 7: Angular location of the crack initiation sites as a function of the interference fit level. The crack initiation location is indicated by a yellow star.

Cracks systematically initiate at the lug bore and propagate in a fairly straight line (with a deviation of $\pm 10^\circ$ from the radial plane) until the failure of the lug. The broken holes tend to fracture in fatigue on only one side of the lug (the other side fails statically) as observed by Fisher and Winkworth [7]. The angular location of the crack initiation sites are measured (to an accuracy of $\pm 1.5^\circ$) and tend to increase with the level of interference fit

(Figure 7), but no trend with the loading level is observed. As the interference fit increases, the crack location moves closer to the equatorial plane (i.e. for $\theta = 90^\circ$) of the lug.

The cracks initiate in the central part of the lug bore, and not at the corners. The fracture surfaces of the broken lugs show dark oxidation spots at the crack initiation sites (Figure 8b and Figure 8e). These spots are typical of fretting contacts [31][32] and are due to Mode II small crack propagation and entrapment of wear debris within the crack lips. These dark crack initiation zones become smaller and more numerous as the interference fit level increases. Up to a certain crack length, Mode I propagation becomes predominant and fatigue striations can be observed at the crack lips (Figure 8d).

Broken and unbroken specimens show surface wear damage at the lug-bush contact surfaces (Figure 8, Figure 9). Due to the geometry of the specimens, analyses are mainly carried out on the bushes. Two types of surface damage are observed on the surface of the bushes, near the crack location. The first, located below the crack front, is “cracking wear” (Figure 9). It is due to the ploughing of the crack lips of the lug against the bush. The second type, also visible above the crack initiation front, corresponds to fretting wear damage prior to crack initiation. It takes the form of a discontinuous distribution of fretting wear patches. Similar wear spot patterns can be observed on the broken and unbroken sides of the lugs (Figure 8, Figure 9). These dark fretting wear spots are caused by the contact pressure and the relative sliding between the lug and the bush. Such irregular distribution of the fretting scars were observed by Knabner [32] and Ozen [14]. This irregular distribution can be explained by the combination of the inherent cylindricity error associated with the finishing operation and the machining grooves. Lewis, Marshall *et al.* [33][34] observed by ultrasound method the pressure distribution of the interference fit assemblies. Since the contact surfaces do not perfectly match, there are peaks and valleys in the pressure distribution at the contact interface. This phenomenon would be enhanced by the shrink fit process which does not plastically deform the surface during assembly [34].

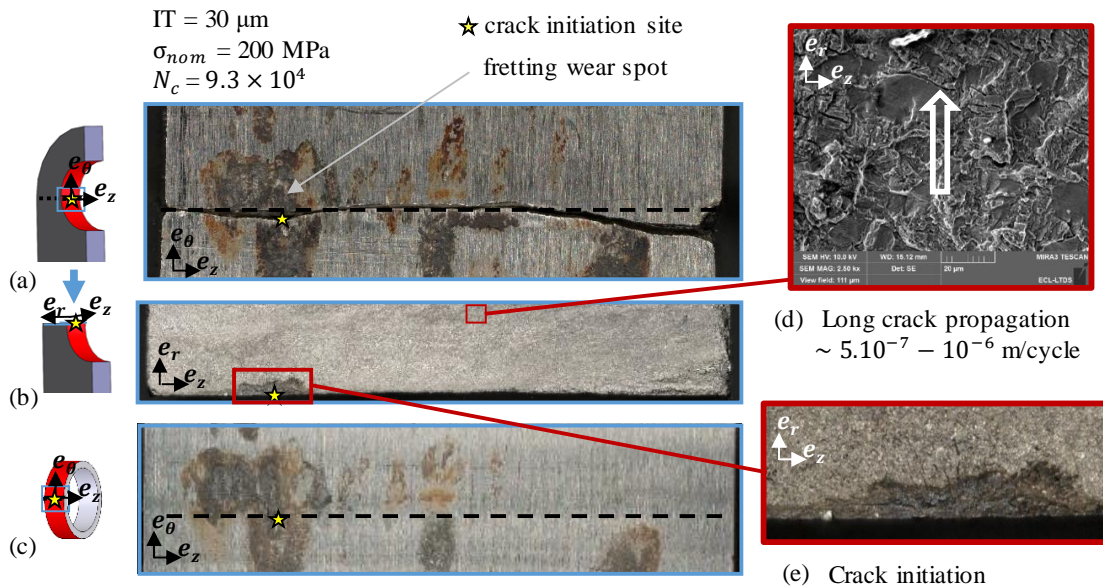


Figure 8: Optical observation of the (a) lug bore surface, (b) lug fracture surface, (c) bush surface at the failure area of a broken specimen and (d) SEM observation of the lug fracture surface showing fatigue striations, (e) crack initiation site on the lug fracture surface ($\sigma_{nom} = 200 \text{ MPa}$, $IT = 30 \mu\text{m}$, $N_c = 9.4 \times 10^4$)

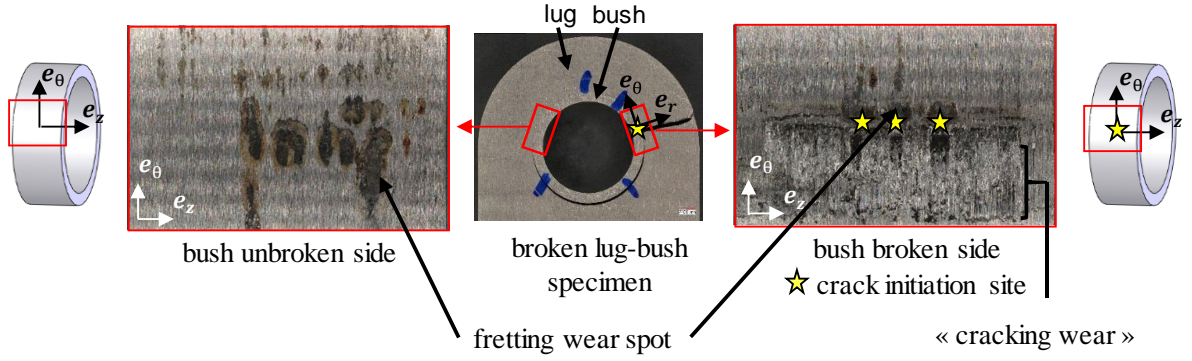


Figure 9: Optical observation of the bush corresponding to the broken hole of a specimen. On the left, observation of the unbroken side and on the right, observation of the broken side of the specimen at the angular position of the crack initiation sites, indicated by yellow stars ($\sigma_{nom} = 175$ MPa, IT = 10 μ m, $N_c = 1.1 \times 10^5$).

In order to assess the effect of surface wear damage on crack initiation, the fracture surfaces of the specimens were systematically compared with the surfaces of the bushes at the fracture zones (Figure 10). There is a strong evidence of a correlation between crack initiation sites and fretting wear spots. Again, only wear damage above the crack initiation site needs to be considered as cracking wear can occur. The correlation between fretting wear spots and crack initiation sites is more obvious for the 10 μ m interference fit level as there are fewer fretting wear spots. It can be noticed that fretting wear spots are present both above and below the fracture zone whereas TA6V-steel lug-bush specimens from Ozen's work [35] show fretting damage only below the crack location.

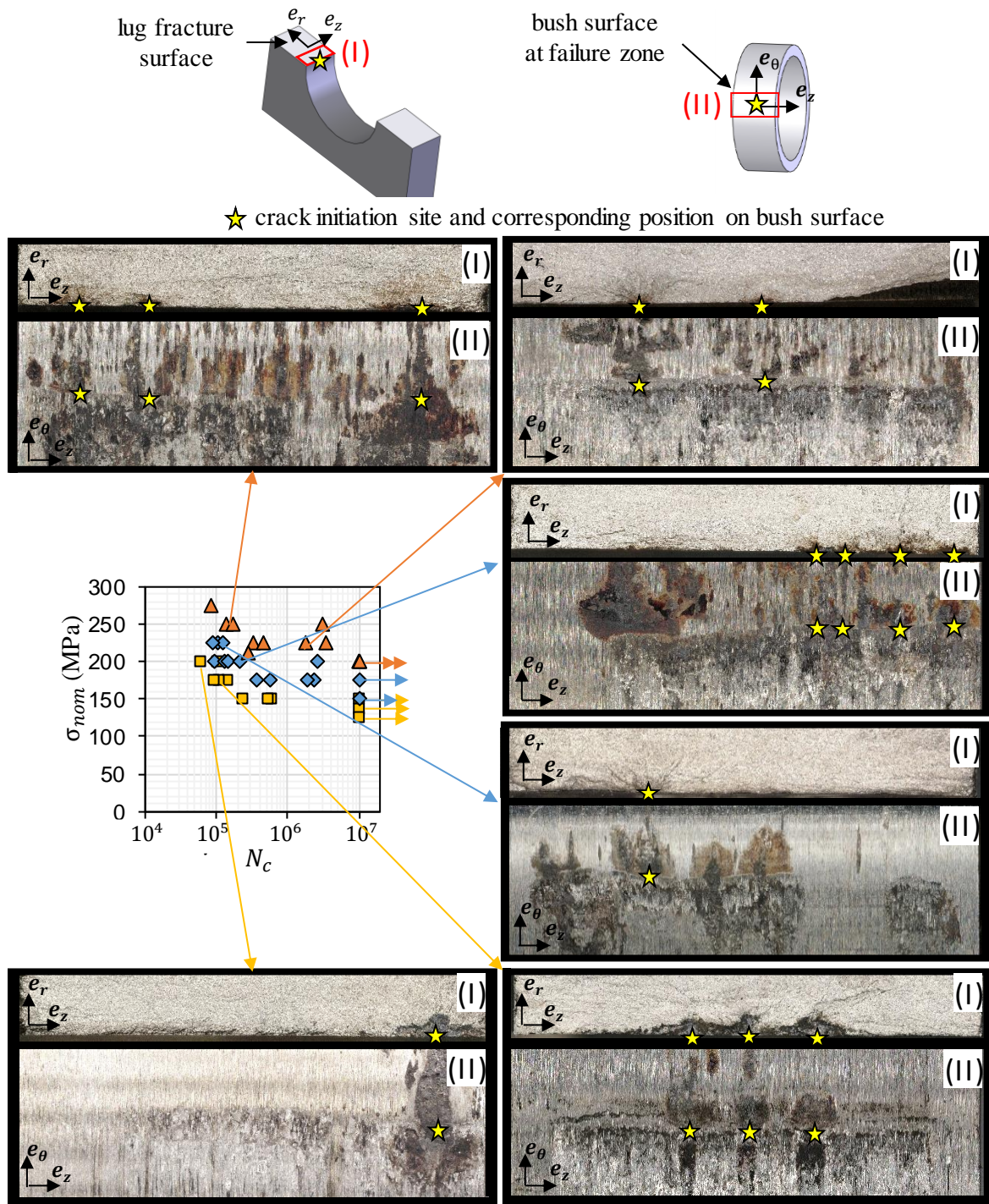


Figure 10: Optical observation of the fracture surfaces and bushes surfaces at the corresponding failure zone for several broken specimens. The crack initiation sites are indicated by yellow stars.

It is interesting to note that the 10 μm interference fit specimens are characterised by tilted (between 5° to 20°) crack initiation angles with respect to the macroscopic fracture plane (the latter being close to the radial plane). The surface profiles of the fracture surfaces of two 10 μm interference fit fractured specimens are shown in

Figure 11, with the corresponding crack initiation angle. No such tilted crack initiation angle is observed for higher interference fit specimens.

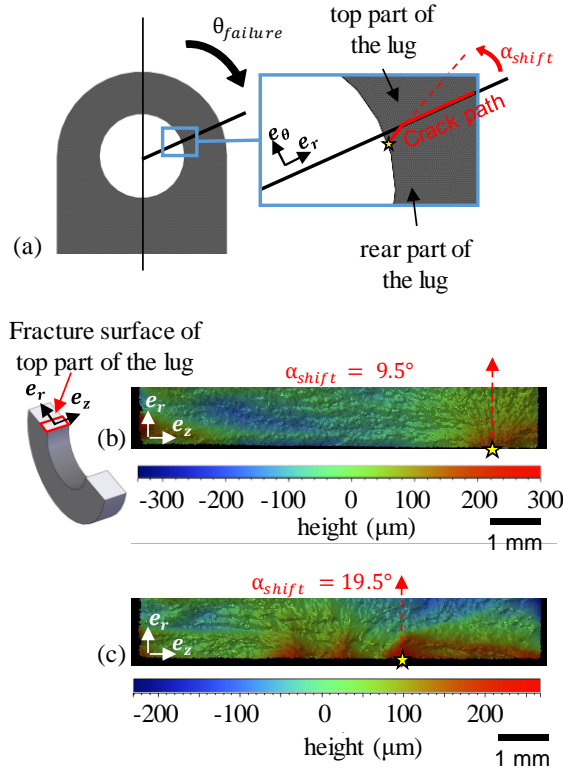


Figure 11 : (a) Description of the observed crack path for the 10 μm interference fit specimens, (b, c) profilometry of the fracture surfaces of the top part of the lugs of two broken specimens corresponding respectively to IT = 10 μm - $\sigma_{nom} = 175 \text{ MPa}$ - $N_{cycle} = 1.1 \times 10^5$ and IT = 10 μm - $\sigma_{nom} = 200 \text{ MPa}$ - $N_{cycle} = 5.9 \times 10^4$.

3.2 Chemical and cross section analysis of fretting wear spots

To observe fretting wear spots within the contact zone, an unbroken specimen was cold mounted prior to sawing to maintain contact between the lug and bush parts (Figure 12). Two types of fretting wear spots are observed at the lug-bush interface.

The first one, called FWS_{Fe} , is composed of oxygen, iron and alloying elements of Maraging 250 (Figure 13a and Figure 13c). The Raman curve of the wear spot shares the typical peaks (700 cm^{-1} , 480 cm^{-1} , 325 cm^{-1}) of NiFe_2O_4 [36] and CoFe_2O_4 [37][38] oxides (Figure 13e).

The second type, called FWS_{Ti} , contains oxygen, titanium and alloying elements of Ti-6Al-4V (Figure 13b and Figure 13d). This type of wear spot has a layered structure consisting of 'pure' Ti-6Al-4V mixed with titanium oxide. The Raman curve (Figure 13f) does not show the typical peaks of titanium dioxide [39][40].

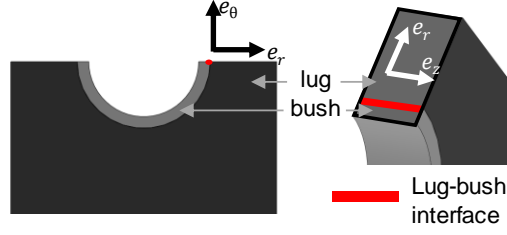


Figure 12: Sample surface observation

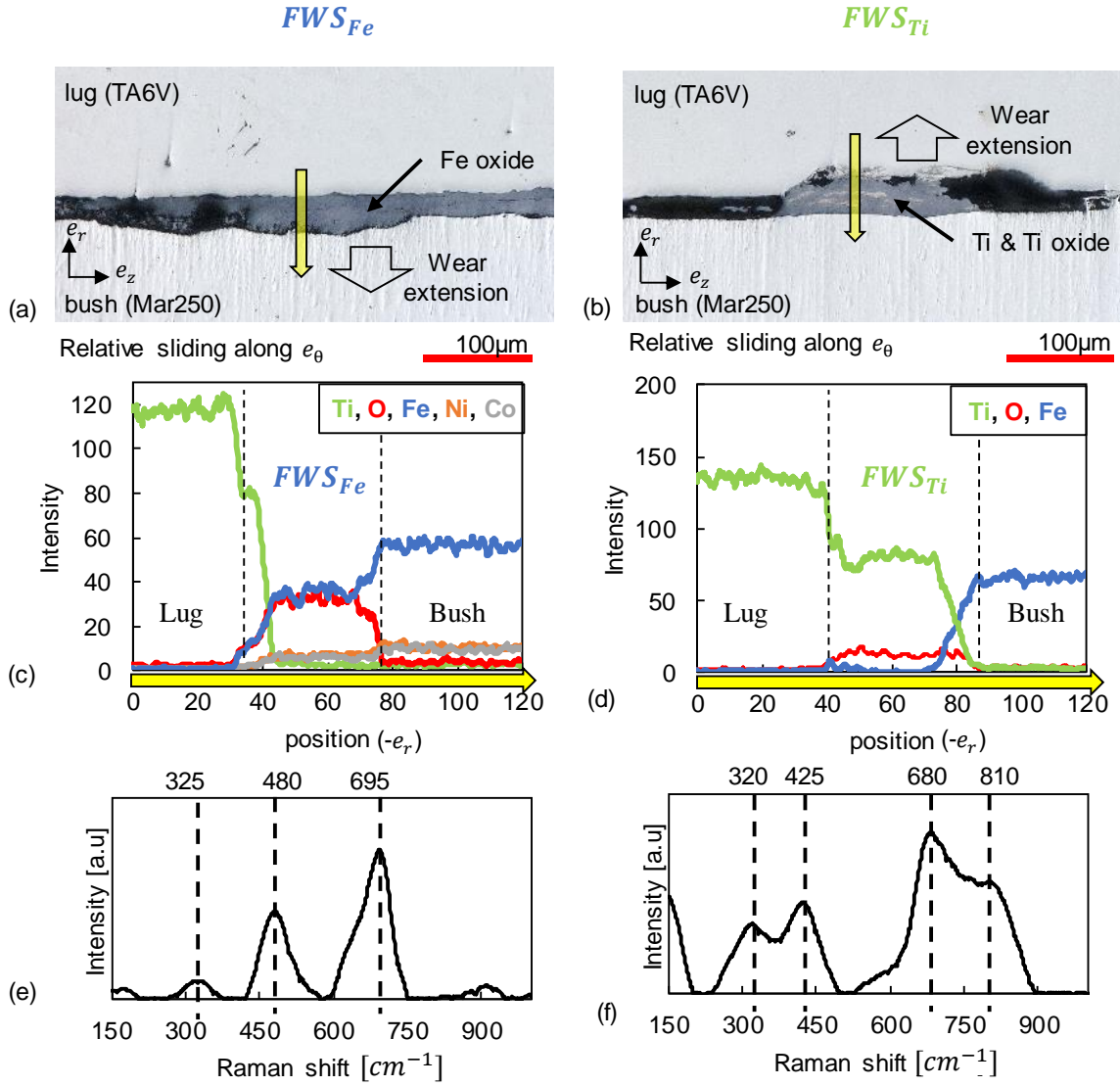


Figure 13 : (a, b) Optical observation, (c, d) EDX line analysis (along yellow arrow) and (e, f) Raman curves of the two types of fretting wear spots composed of respectively Fe oxides (a, c, e) and titanium oxides (b, d, f) at the lug-bush interface of the unbroken hole of a tested specimen ($\sigma_{nom} = 250 \text{ MPa}$, $IT = 50 \mu\text{m}$, $N_{cycle} = 1.4 \times 10^5$)

Fretting wear consist in entrapped agglomerates of oxidised wear debris. After opening of the contact, it is observed that the titanium oxides tend to adhere to the steel bushes while the iron oxides tend to adhere to the titanium alloy lugs causing pits and humps on the bushes surface, respectively, as observed in Figure 14.

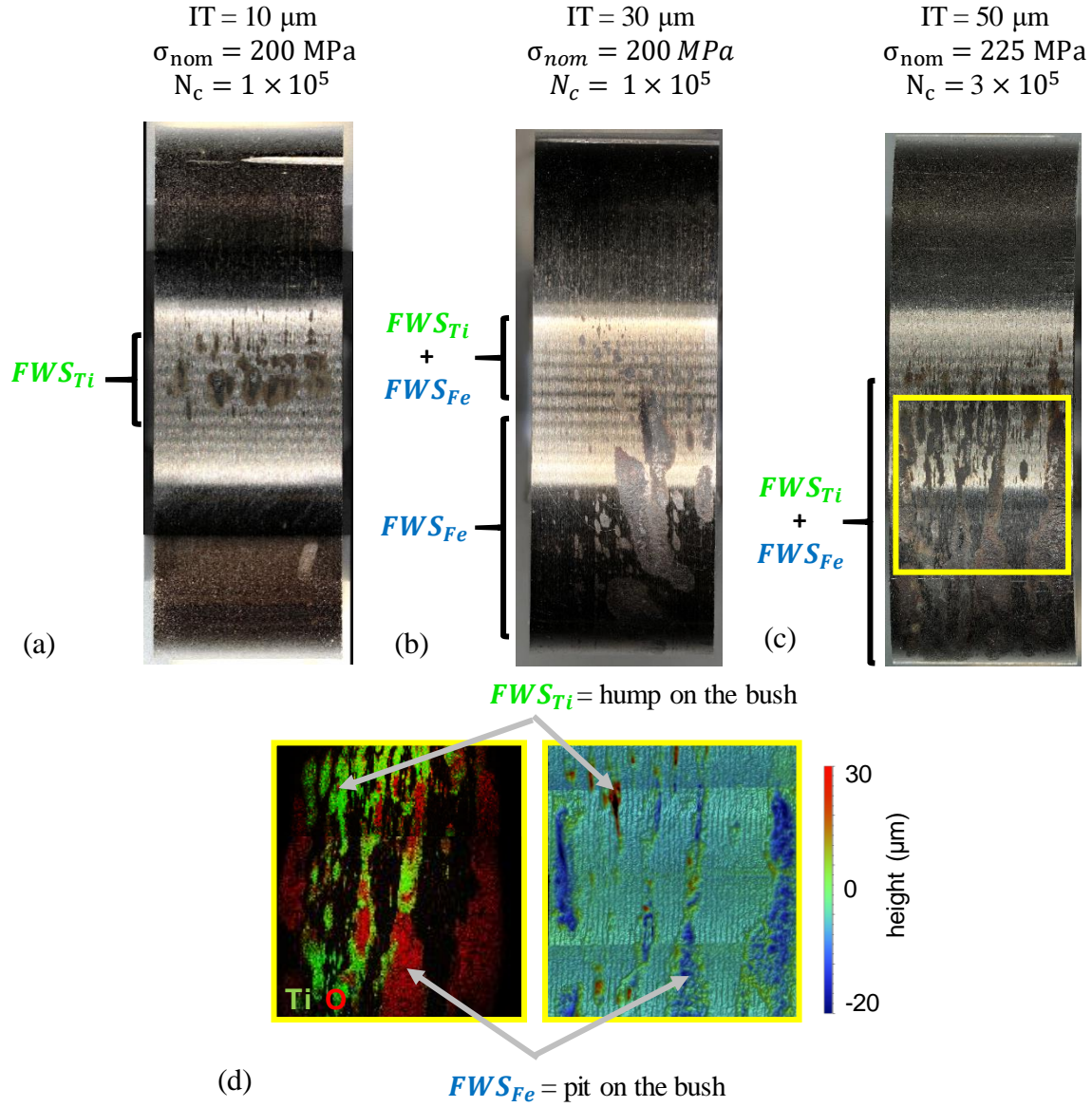


Figure 14: (a, b, c) Optical observation of the unbroke side of the bush of three tested specimen (b) EDX map analysis showing the presence of titanium and oxygen elements and profilometry analysis of the bush surface of a 50 μm interference fit specimen.

The distribution of wear damage is highly sensitive to the interference fit. For a low interference fit, the surface damage is localised to the side part of the interface whereas for a higher interference fit, it extends from the side to the rear of the lug-bush interface. The formation of FWS_{Ti} is confined to the upper side area for 10 μm and 30 μm interference fit specimens while FWS_{Ti} is also observed on the rear part of the interface for 50 μm interference fit specimens. The size of the iron oxide wear spots increases and becomes predominant over FWS_{Ti} as the number of loading cycles increases.

Only a small amount of detached wear debris is observed after fatigue tests and contact opening. Wear loss was barely measurable and is therefore assumed to be negligible.

It is possible to reconstruct the lug-bush interface after opening of the contact. An example is shown in Figure 15. The height profiles of a lug and a bush were measured by interferometry along a horizontal band, showing Ti oxide fretting wear spots, and were then superimposed. The height profiles at the fretting spot sites matched well and a gap of few microns was observed between the lug and the bush in undamaged areas.

The lug-bush contact interface is clearly discontinuous with the presence of fretting oxide patched between near undamaged surfaces (machining grooves are visible). It should be noted that the specific volume of the oxides is generally more important than that of the base material. These oxidised wear spots correspond to localised additional volumes of material at the lug-bush interface which would probably cause discontinuity in the lug-bush clearance and consequently localised overpressures.

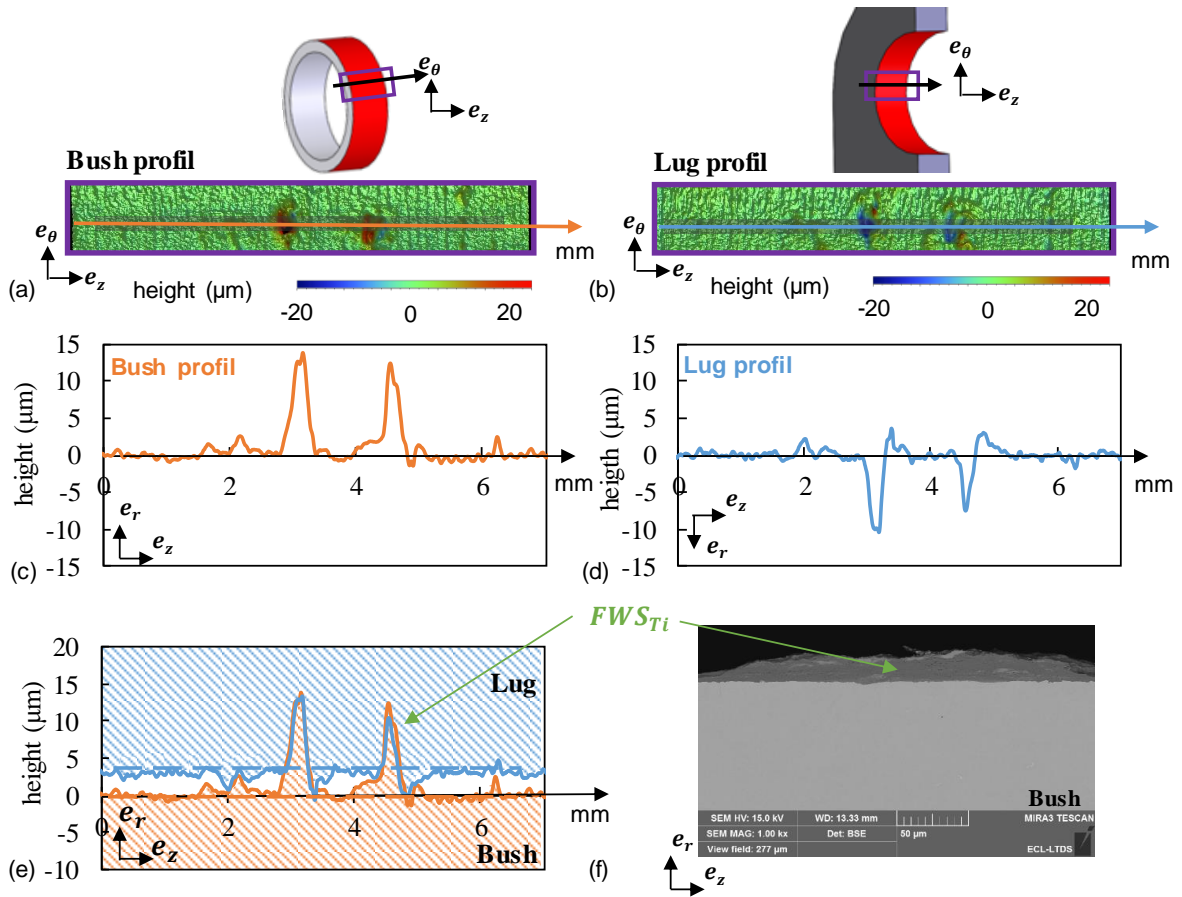


Figure 15: (a) Front view of a bush profile, (b) front view of a lug profile, (c) bush profile height along the orange line of picture (a), (d) lug profile height along the blue line of picture (b), (e) superposition of lug and bush height profiles, (f) SEM observation of a fretting wear spot on the bush ($\sigma_{nom} = 200$ MPa, IT = 10 μm,

$$N_{cycle} = 1.0 \times 10^5)$$

3. Numerical investigation

Numerical analysis is used to estimate the stress-strain state and local tribological loading at the lug bush interface.

4.1 Numerical model:

2D and 3D finite element analyses are carried out using Abaqus software (Figure 16a and Figure 16b). Due to the symmetries, $\frac{1}{4}$ of the system is considered. For the 3D model, eight-node reduced integration elements (C3D8R) are used, with a penalty tangential contact behaviour with a maximum allowed elastic slip of $0.5 \mu\text{m}$ (to compensate for convergence problems). For the 2D model, the plane stress assumption is used with CPS4R node reduced elements and a Lagrangian augmented tangential contact behaviour.

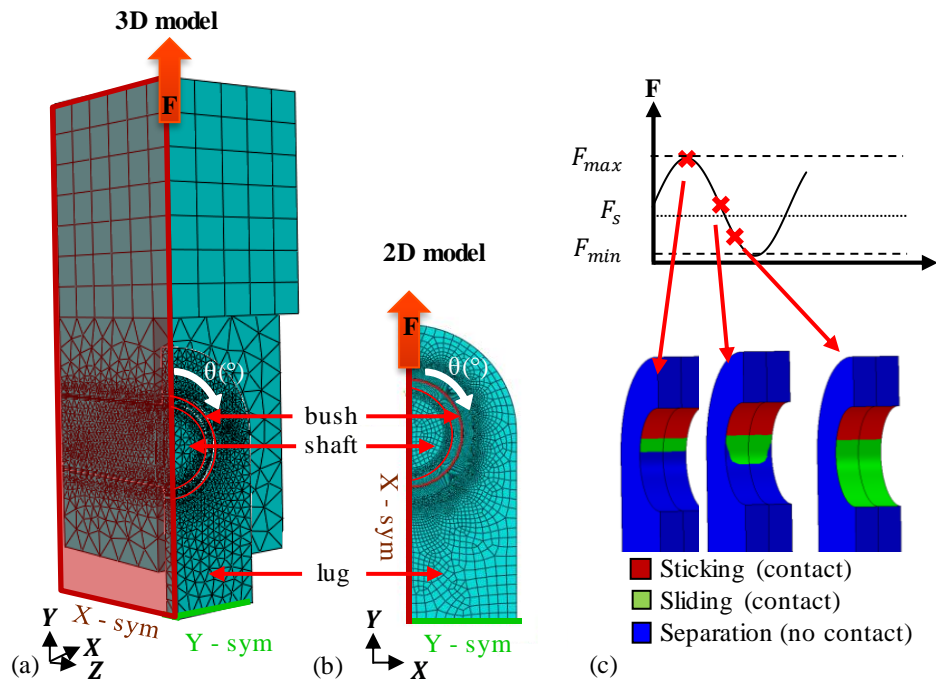


Figure 16: (a) 3D and (b) 2D numerical models, (c) applied loading and corresponding contact state evolution at the lug-bush interface

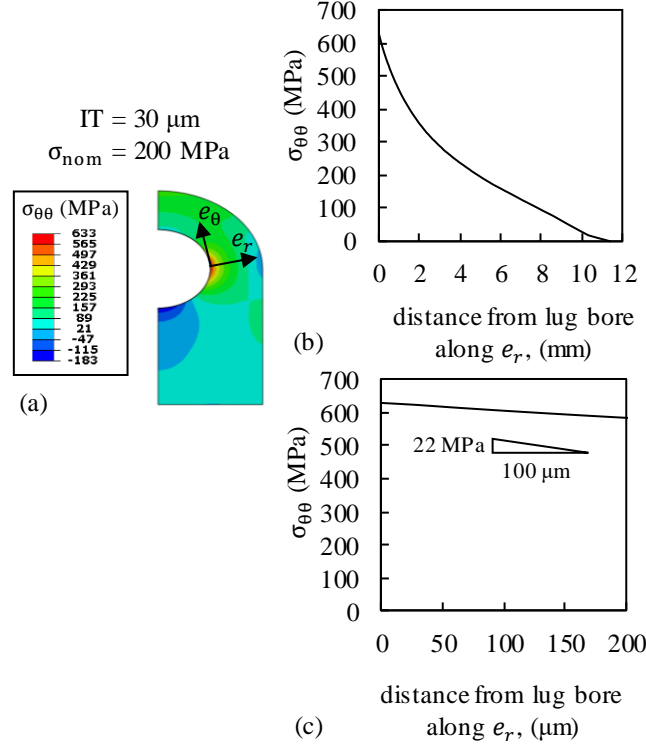


Figure 17 : (a) Orthoradial stress ($\sigma_{\theta\theta}$) distribution on the lug bore, (b, c) $\sigma_{\theta\theta}$ evolution along the radial direction (e_r) from the hot spot at the lug bore. Mesh size = 25 μm , 2D plane strain, $\sigma_{nom} = 200$ MPa, $IT = 30$ μm , $C = 100$ μm , $\mu_{bush-shaft} = 0.1$, $\mu_{lug-bush} = 0.25$

The interference fit is simulated by initial geometric interpenetration of the lug and bush. Elastic behaviour is used with material parameters E and ν given in Table 3. We take as a first approach $\mu_{lug-bush} = 0.25$ corresponding to an undamaged metal-metal contact [41] and $\mu_{bush-shaft} = 0.1$ representing a greased interface as the pin was greased prior testing.

A static analysis is performed with a discretization in 80 steps of each loading cycle. The strain-stress distribution is observed after the second loading cycle. For each specimen, the measured bush and lug diameters are taken into account for the simulation as the interference fit has a strong effect on the stress distribution [10]. As in the experimental tests, a sinewave loading is applied with a load ratio of 0.1. The stress is maximised at the lug bore (Figure 17a and Figure 17b). Due to the rather low stress gradient (Figure 17c), a mesh refinement of 0.1 mm at the lug-bush interface was considered to be consistent, and is used in the following simulations.

4.2 Damage criteria:

Several criteria are considered and implemented using a Python script.

4.2.1 Tribological criterion (friction energy density parameter)

The sticking/sliding and sliding/opening fronts evolve with loading. The front part of the lug bore remains in a sticking state, while the lug and the bush slide against one another on the side part of the interface (Figure 16c).

In this way, the system can be considered in a partial slip regime [42]. The pressure distribution also evolves with the load and the lug and bush can separate at a sufficient load value (F_s) (Figure 16c).

To account for the evolving tribological load, integral formulations of the relative sliding amplitude and the friction energy density are adopted.

The relative sliding amplitude per cycle Δ_s is defined as:

$$\Delta_s [\mu m] = \frac{1}{4} \int_{cycle} |d\delta| \quad (3)$$

The principal sliding direction (CSLIP1) is along e_θ and the second sliding direction, for the 3D model, is along e_z (CSLIP2)). The implemented definition of the relative sliding amplitude is as follows:

$$\Delta CSLIP1_n = |CSLIP1_n - CSLIP1_{n-1}| \quad (4)$$

$$\Delta_s = \frac{1}{4} \sum_{n=1}^{n=N_{timestep}} \Delta CSLIP1_n \quad (5)$$

The surface density of the frictional energy dissipated per cycle φ [mJ/mm²], defined as the density of frictional work, is the product of the shear stress τ and the relative sliding δ .

$$\varphi [mJ/mm^2] = \int_{cycle} |\tau| \cdot |d\delta| \quad (4)$$

The main shear direction (CSHEAR1) is along e_θ and the second shear direction, for the 3D model, is along e_z (CSHEAR2)). The implemented definition is as follows:

$$CSHEAR1_{mean, n} = |\frac{1}{2}(CSHEAR1_n + CSHEAR1_{n-1})| \quad (5)$$

$$\varphi_{cycle} = \sum_{n=1}^{n=N_{timestep}} CSHEAR1_{mean, n} \times \Delta CSLIP1_n \quad (6)$$

In 3D, φ_{cycle} is the sum of the contribution of the two sliding directions.

The surface friction energy density parameter is widely used to quantify the fretting wear phenomenon [43], but it is also considered by Ruiz's approach to quantify fretting cracking damage [44].

4.2.2. Multiaxial fatigue stress criterion

The Smith, Watson and Topper multiaxial fatigue critical plane extension criterion [45] is tested. It is a critical plane stress criterion based on the Mode I mechanism for crack initiation. The critical plane is determined by maximising a damage parameter. The latter is defined for a plane of normal \vec{n} as the product between the maximum tensile stress $\sigma_{max}(\vec{n})$ normal to the plane \vec{n} and the strain amplitude $\varepsilon_a(\vec{n})$ normal to the plane \vec{n} (in our case, \vec{n} remains in the (X, Y) plane).

$$\Gamma_{SWT, n} = \max_{\vec{n}} \sigma_{max}(\vec{n}) \cdot \varepsilon_a(\vec{n}) \quad (7)$$

Assuming a linear elastic behaviour, an equivalent stress can be determined using the following formula:

$$\sigma_{SWT, n} [MPa] = \max_{\vec{n}} \sqrt{E \sigma_{max}(\vec{n}) \cdot \varepsilon_a(\vec{n})} \quad (8)$$

This equivalent stress can be compared with the material alternating stress fatigue data.

4.2.3. 2D/3D comparison

Due to the small width of the specimens (8 mm) and the negligible bending of the shaft, the plane stress hypothesis is consistent. Close shrink-fit contact pressure, orthoradial stress and strain distributions at the lug bore are obtained by comparing 2D model with the mid-plane of the lug bore in the 3D model (Figure 18). The maximum contact pressure in the mid-plane of the lug bore is lower for the 3D model compared to the 2D model due to the low bending of the shaft.

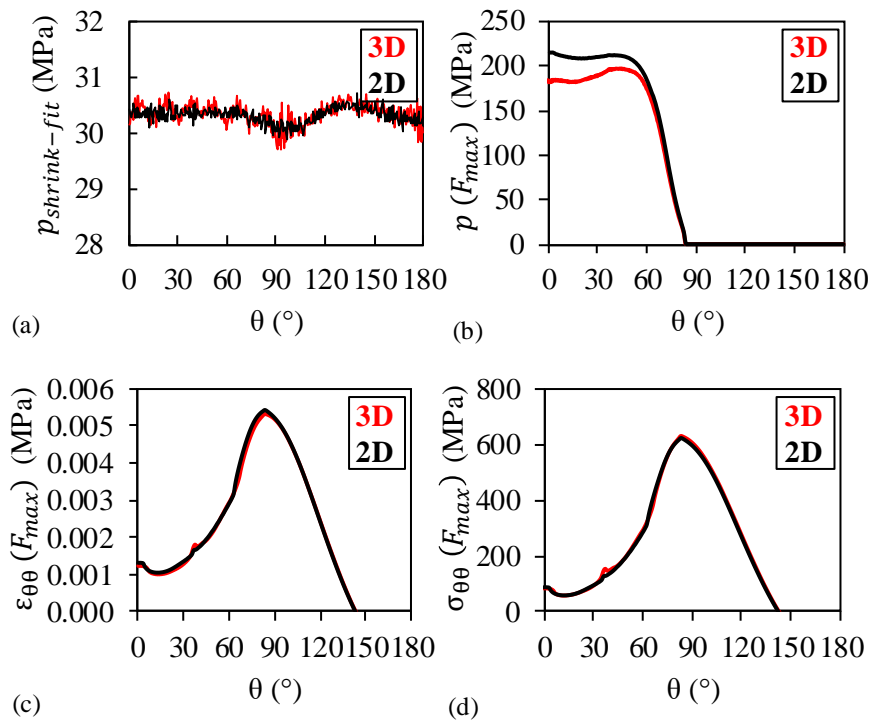


Figure 18 : Distribution of the (a) interference fit contact pressure, (b) contact pressure at maximum loading (b) orthoradial strain at maximum loading, (c) orthoradial stress at maximum loading along the vertical middle plane of the lug bore for a 3D model and a 2D plane stress model. Mesh size = 100 μm , $\sigma_{nom} = 200$ MPa, IT = 30 μm , C = 100 μm , $\mu_{bush-shaft} = 0.1$, $\mu_{lug-bush} = 0.25$

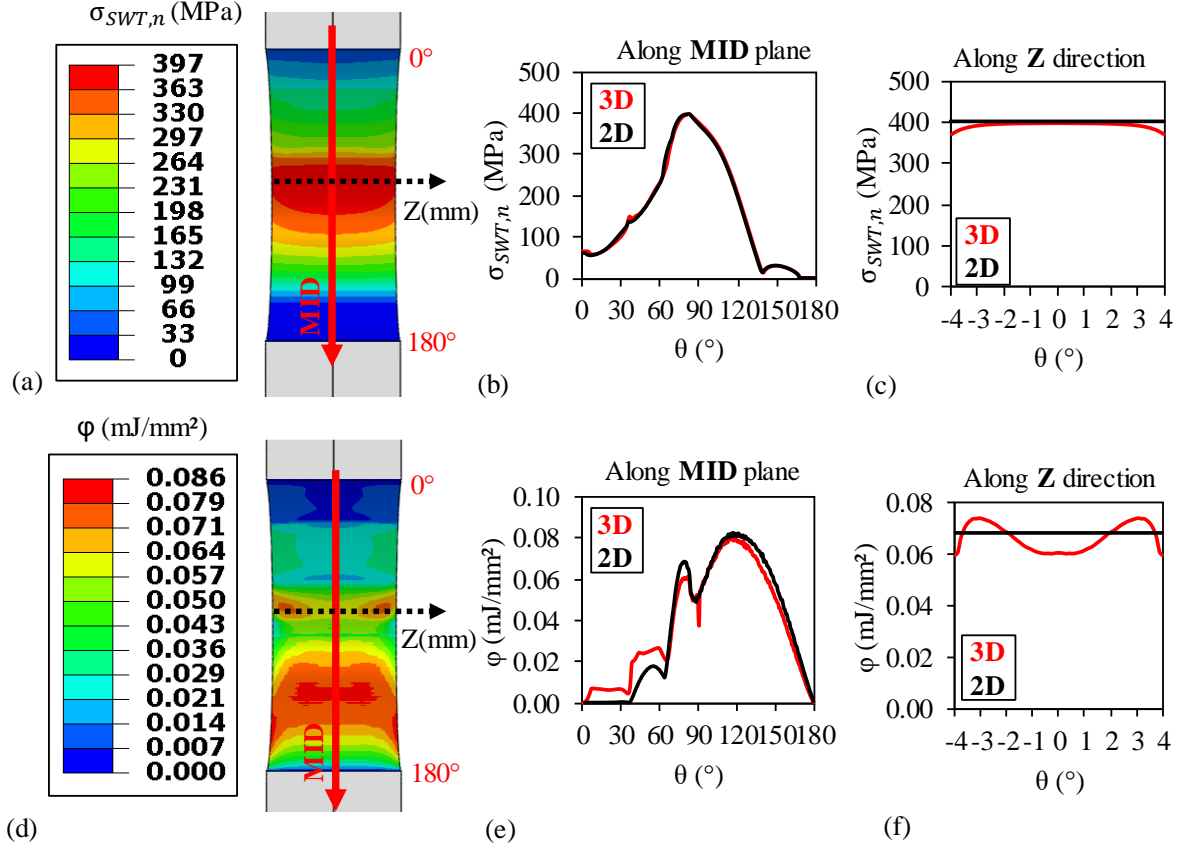


Figure 19: (a, d) Distribution of the SWT equivalent stress (σ_{SWT}) and the dissipated friction energy density (φ) along the lug bore for a 3D model, (b,e) distribution of the SWT equivalent stress (σ_{SWT}) and the dissipated friction energy density (φ) along the vertical mid plane of the lug bore for a 3D model and 2D plane stress model, (c, f) distribution of the SWT equivalent stress (σ_{SWT}) and the dissipated friction energy density (φ) along the horizontal direction (Z) of the lug bore for a 3D model and 2D plane stress model. Mesh size = 100 μm , $\sigma_{nom} = 200 \text{ MPa}$, IT = 30 μm , C = 100 μm , $\mu_{bush-shaft} = 0.1$, $\mu_{lug-bush} = 0.25$

The SWT equivalent stress (σ_{SWT}) and the dissipated friction energy density (φ) (Figure 19) obtained along the mid-plane of the lug either by considering a 3D modelling or by considering a 2D approximation in plane stress are close.

It should be noted that the elimination of the chamfers by machining of the faces, to produce an edge-to-edge configuration, completely eliminates the discontinuities on the lateral edges so that the maximum of the stress is found in the centre of the lug bore (Figure 19c). This result is in agreement with the experimental results which indicate that cracks initiate in the central part of the lug bore.

4.2.4 Distribution of the criteria

The distributions of orthoradial stress ($\sigma_{\theta\theta}$), SWT equivalent stress (σ_{SWT}), contact pressure at the maximum loading (p), relative sliding amplitude (Δs), and the surface density of the dissipated energy (ϕ) are represented in Figure 20 for the three levels of interference fit and for the different loading levels tested. An allowance of 100 μm between shaft and bush prior shrink fitting is considered.

For this configuration, the nominal stresses for the lug-bush separation are 46, 120, 192 MPa for 10 μm , 30 μm and 50 μm interference fit levels respectively. At a sufficiently high loading, the angular location of the lug-bush separation stabilises and the separation angles are 80°, 85° and 90° for 10 μm , 30 μm and 50 μm interference fit specimens respectively (red dotted line in Figure 20). It should be noted that separation angles below 90° are achieved due to the large clearance between the shaft and the bush.

The orthoradial and SWT equivalent stresses tend to be maximum at the lug-bush separation angle, which also corresponds to the range of the angular locations of crack initiation for the different interference fit specimens.

The relative sliding between the lug and the bush and the surface density of friction energy dissipated per cycle do not follow a linear evolution with loading. Surprisingly, the relative sliding amplitude is more important for higher interference fits. This is because the load required to open the contact between the lug and the bush is less for lower interference fit levels. Then for low interference fit specimens, the lug and bush separate quickly [42]. Therefore, there is limited time for the lug and bush to slide on against each other. This phenomenon is due to ovalisation of the bush and is exacerbated, in our case, by the low stiffness of the bush and the high clearance fit between the shaft and bush.

The surface damage of the bushes correlates well with the distributions of the sliding amplitude and the surface density of friction energy dissipated per cycle. The front part of the bushes is systematically free of damage because lugs and bushes remain stuck together. Unlike the 30 μm and 50 μm interference fit specimens, the rear zone of the bushes with 10 μm interference fit is also free of visible surface damage because the surface density of friction energy dissipated per cycle is low (Figure 14).

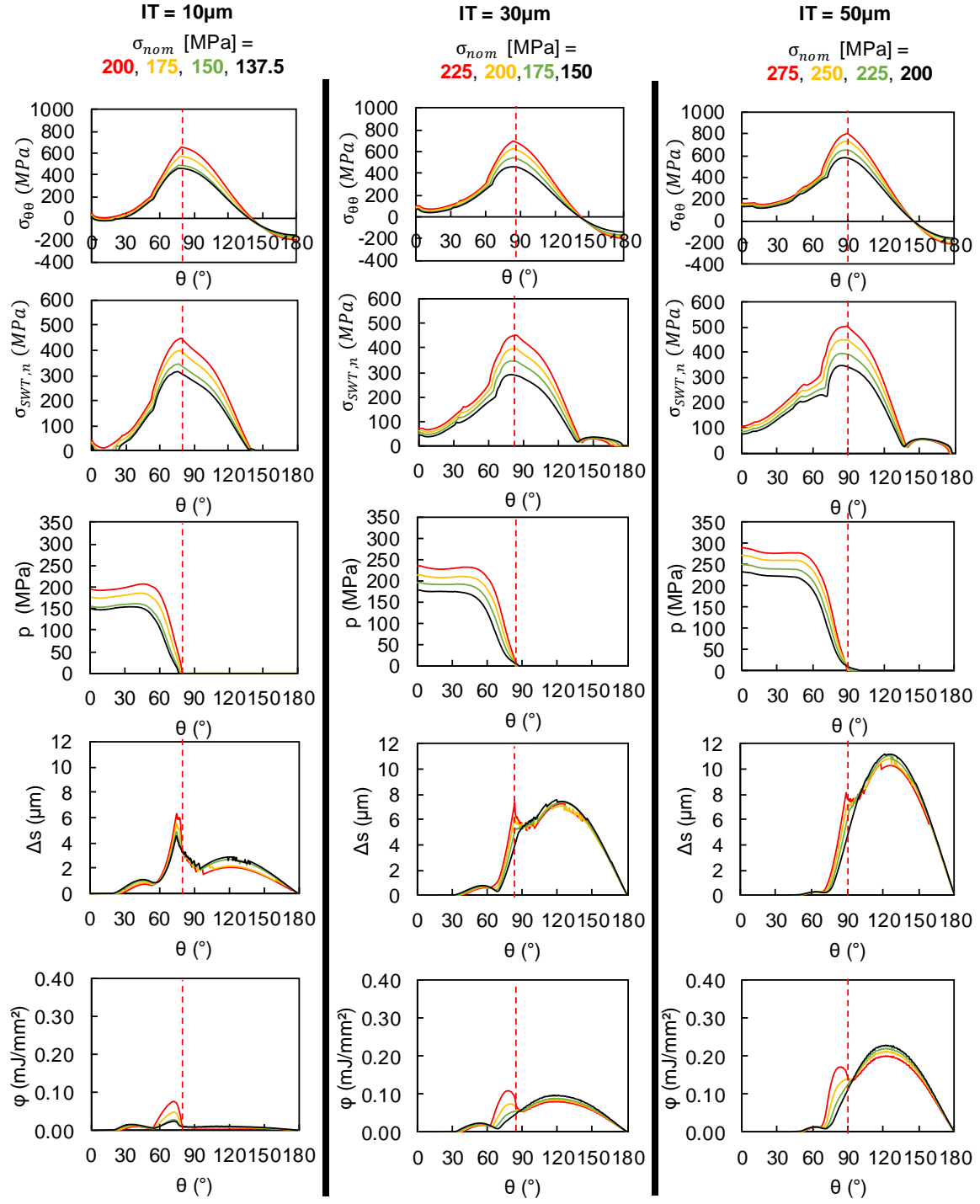


Figure 20: Distribution of orthoradial stress ($\sigma_{\theta\theta}$), SWT equivalent stress (σ_{SWT}), contact pressure at maximum loading (p), amplitude of relative sliding (Δ_s), surface density of dissipated energy (ϕ) along lug bore for different loading levels and for the three levels of interference fits. Mesh size = 100 μm, 2D plane stress, $C = 100$

$$\mu_m, \mu_{bush-shaft} = 0.1, \mu_{lug-bush} = 0.25$$

4.3 Plain SWT fatigue stress analysis (σ_{SWT})

4.3.1 Homogeneous low coefficient of friction

A first approach is to exclude the potential effect of wear damage on crack initiation. The multiaxial SWT criterion is used to estimate the risk of crack initiation due local stress-strain loading. The maximum of the SWT equivalent stresses of all specimens tested are plotted in an $\sigma_{SWT,n_{max}}-N_c$ graph (Figure 21a) to be compared with the reference Ti-6Al-4V fatigue data [28]. All points are gathered along a single master curve with a discrepancy of about 100 MPa compared to the reference material fatigue data. It should be noted that there are some scatter points with higher fatigue life than the general trend, mainly for the largest values of interference fit (dotted circle in Figure 21a).

The predicted angular crack initiation locations are also compared with the experimental results in Figure 21b. The general increasing trend of the cracking angular location with the interference fit is also observed numerically. The SWT critical planes were found to be close to the radial plane (with an approximate shift of 5°) regardless of the level of the interference fit (Figure 22).

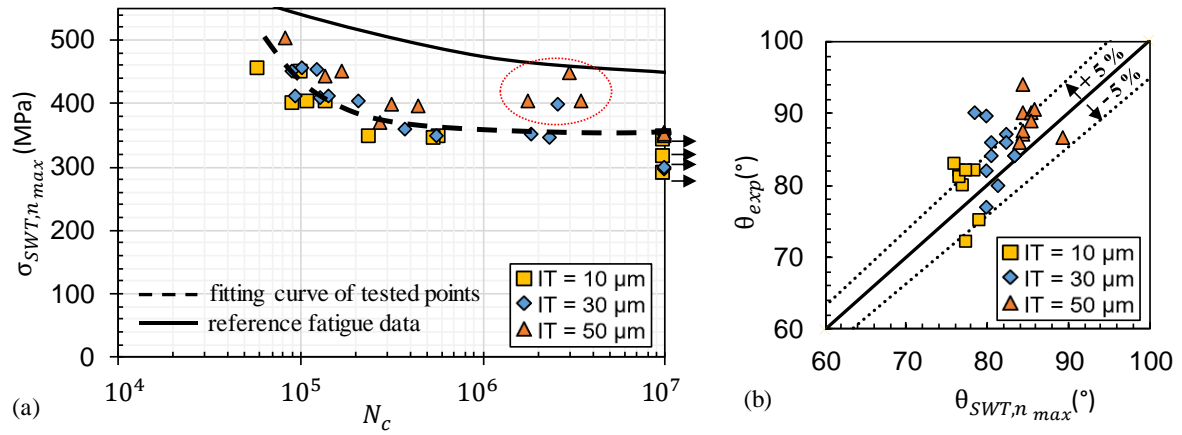


Figure 21: (a) Evolution of the SWT equivalent stress ($\sigma_{SWT,n_{max}}$) of the tested specimens with the number of cycles to failure, (b) comparison between experimental angular crack initiation positions and SWT prediction.

Mesh size = 100 μm , 2D plane stress, $\mu_{bush-shaft} = 0.1$, $\mu_{lug-bush} = 0.25$

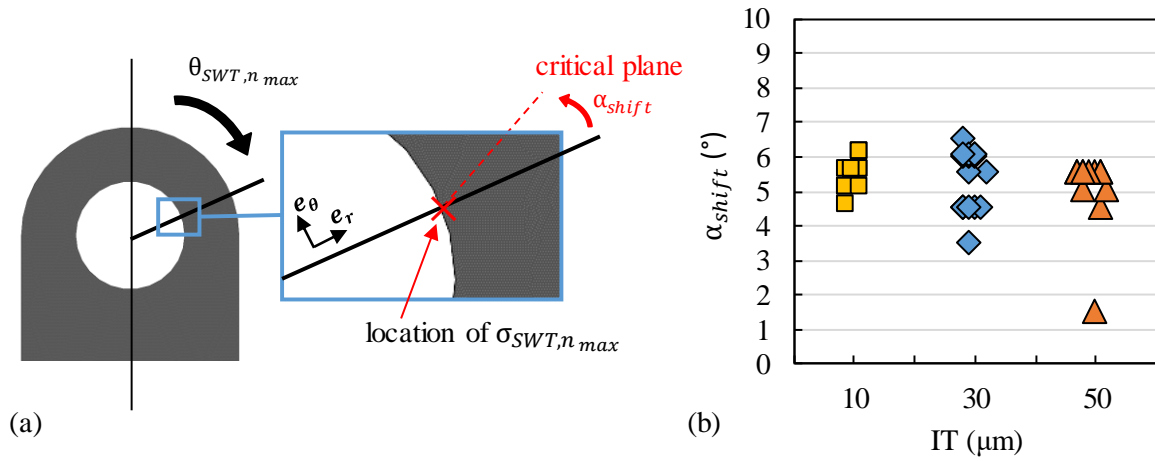


Figure 22 : (a) Description of α_{shift} and (b) α_{shift} of the tested specimens according to interference fit levels.

Mesh size = 100 μm, 2D plane stress, $\mu_{bush-shaft} = 0.1$, $\mu_{lug-bush} = 0.25$

For all the specimens, the difference between the value of the maximum equivalent stress as derived from the SWT critical plane criterion ($\sigma_{SWT, n_{max}}$) or from the modified SWT criterion where a radial plane is imposed as the critical plane ($\sigma_{SWT, e_{\theta} max}$) is less than 5 MPa. The stress state at the lug bore is driven by the orthoradial stress.

Analysis of the contribution of the maximum stress and strain amplitudes of the calculated equivalent stresses $\sigma_{SWT, e_{\theta} max}$ of the specimens tested for the different interference fit levels highlights the beneficial effect of the interference fit on fatigue life. Considering $\sigma_{SWT, e_{\theta} max} = \sqrt{\sigma_{\theta\theta} E \varepsilon_{a, \theta\theta}}$, the relative maximum SWT equivalent stress $\frac{\sigma_{SWT, e_{\theta} max}}{\sigma_{nom}}$, the relative corresponding orthoradial stress $\frac{\sigma_{\theta\theta}}{\sigma_{nom}}$ and relative strain amplitude times Young modulus $\frac{E \varepsilon_{a, \theta\theta}}{\sigma_{nom}}$ are plotted for all tested specimens according to their interference fit levels (Figure 23). As the interference fit decreases, so does the orthoradial stress, strain amplitude and SWT equivalent stress.

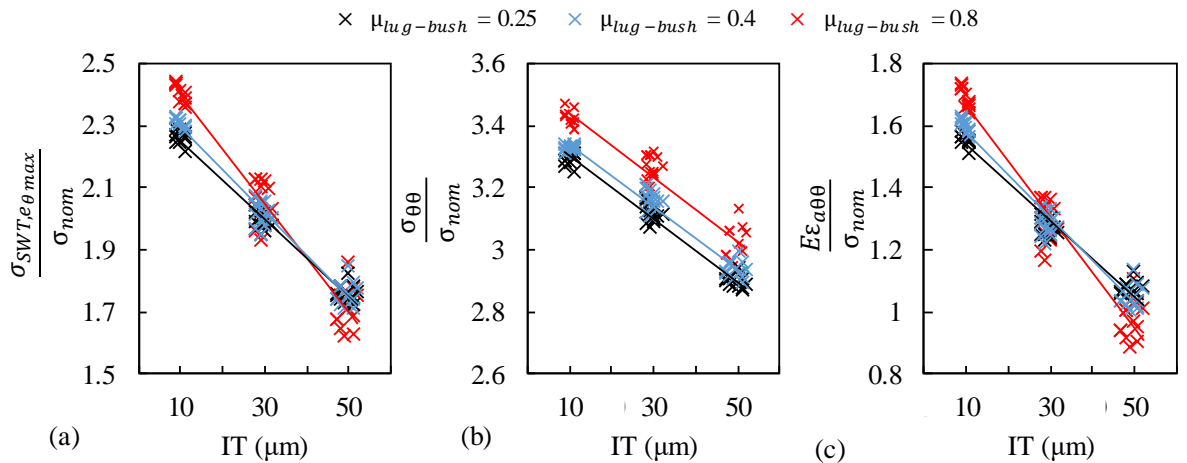


Figure 23 : Considering the SWT critical plane criterion with a radial plane critical plane

$\sigma_{SWT, e_{\theta} max} = \sqrt{\sigma_{\theta\theta} E \varepsilon_{a, \theta\theta}}$, (a) maximum equivalent SWT stress over nominal stress $\frac{\sigma_{SWT, e_{\theta} max}}{\sigma_{nom}}$, (b) orthoradial stress over nominal stress $\frac{\sigma_{\theta\theta}}{\sigma_{nom}}$, (c) strain amplitude times Young modulus over nominal stress $\frac{E \varepsilon_{a, \theta\theta}}{\sigma_{nom}}$ according to interference fit levels and for 3 different friction coefficients at the lug bush interface ($\mu_{lug-bush}$). Mesh size = 100 μm , 2D plane stress, C = 100 μm , $\mu_{bush-shaft} = 0.1$

The SWT criterion captures the mean stress effect and makes it possible to group the tested points on a master curve. However, this master curve is far from the material's fatigue curve. Several explanatory factors need to be taken into account.

It is known that the fatigue behaviour of the Ti-6Al-4V alloy is highly dependent on microstructure, thermomechanical treatment and machining techniques [46]. The data collections carried out by Wu [46] and Bellecave [47] show the HCF strength of Ti-6Al-4V from different articles and the Hines's fatigue data was chosen because of its close microstructure to the material used in this work. Therefore, some uncertainty may need to be considered when using these reference data.

However, such a discrepancy between lug fatigue life and material fatigue strength has already been observed for pin-lug assemblies [48][49][50]. The discrepancy is notable for high numbers of cycles ($> 10^5$ cycles) and Schijve *et al.* [49] and White [50] explain it as being due to both size effect and fretting effect.

Several authors [51][50][49] have tested geometrically similar lugs with the same stress concentration factor but different sizes, and found that the larger lugs (with consequently larger relative movements of sliding) have a much lower fatigue life than the smaller ones. The size effect was not fully understood but they argued that this difference in fatigue life could not be explained by the size effect alone (in the context of Weibull's statistical theory of strength [51]) and then suggested that part of the reduction in fatigue life was due to fretting.

In the following, we will focus on the possible effects of the fretting wear on crack initiation and its modelling.

4.3.2 Homogeneous high coefficient of friction

As a first approach, it was decided to characterize the effect of increasing the coefficient of friction at the lug-bush interface. The maximum stress and strain amplitudes appear to be much less sensitive to the friction coefficient than to the interference fit as observed by Rao [42] (for pin-lug assembly) and Amargier [11] (for interference fitted lugs). As shown in Figure 23, the friction coefficient slightly increases the orthoradial stress (an increase of about 6% in orthoradial stress is observed for an increase in friction coefficient from 0.25 to 0.8) and its effect on strain amplitude depends on the degree of interference fit. An increase in strain amplitude with the friction coefficient is observed for low levels of interference fit, and the opposite is observed for high levels of interference fit. The evolution of the equivalent SWT stress is then less sensitive to the coefficient of friction compared to the interference fit.

A coefficient of friction of 0.8 at the lug-bush interface was tested (Figure 24), which corresponds to the estimated coefficient of friction of a fretting damaged surface (Figure 4). The calculated points are again far from the reference data.

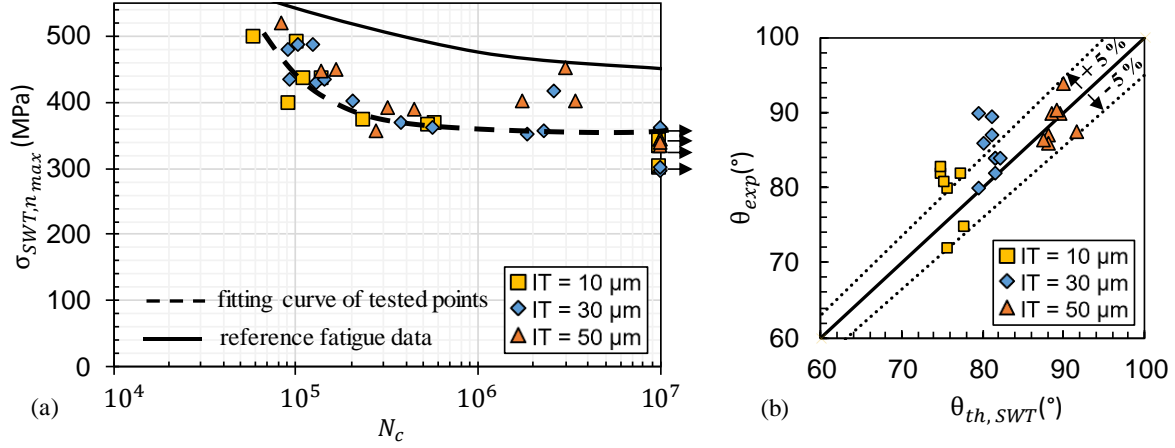


Figure 24 : (a) Evolution of the SWT equivalent stress ($\sigma_{SWT,n_{max}}$) of tested specimens with the number of cycles to failure, (b) comparison between experimental angular crack initiation position and SWT prediction.

Mesh size = 100 μm , 2D plane stress, $\mu_{bush-shaft} = 0.1$, $\mu_{lug-bush} = 0.8$

A parametric study was carried out by varying the coefficient of friction from 0.25 to 3 for a loading condition $\sigma_{nom} = 200$ MPa, IT = 30 μm . Figure 25 shows the corresponding evolution of the $\sigma_{SWT,n}$ profiles. It is interesting to note that despite the large variation in the coefficient of friction, the maximum value of $\sigma_{SWT,n}$ remains well below the fatigue strength of the material. Therefore, even a very large increase in the coefficient of friction cannot explain either the discrepancy with the fatigue life curve or the scatter of the experimental results. This analysis suggests that a homogeneous description of the coefficient of friction within in the interface is not sufficient to describe the physics of the fretting phenomenon involved in the shrink-fit interface of lug-bush assemblies.

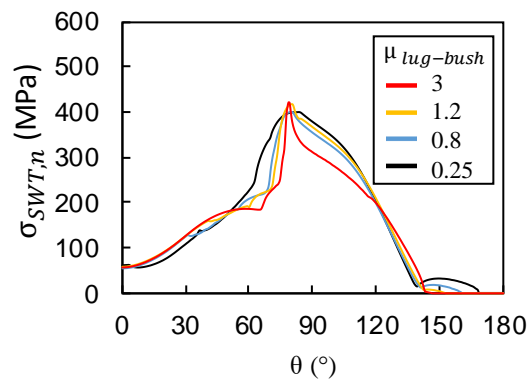


Figure 25 : Distribution of the SWT equivalent stress ($\sigma_{SWT,n}$) along the lug bore for different coefficients of friction. Mesh size = 100 μm , 2D plane stress, $C = 100 \mu\text{m}$, $\mu_{bush-shaft} = 0.1$

4.3.3 Heterogeneous coefficient of friction

Another model was tested by considering fretting wear spots. This was done by modelling a heterogeneous coefficient of friction at the lug-bush interface.

On a $\frac{1}{4}$ simplified 3D model (Figure 26), two areas with different frictional behaviour ($\mu_{FEM(FWS)}$) from the whole lug-bush interface (μ_0) are considered. These areas are located in the identified failure zone of the lug (close to the sliding-opening front at maximum loading) to simulate the presence of fretting wear spots. Different coefficients of friction ($\mu_{FEM(FWS)}$) are tested on these spot locations (Figure 27).

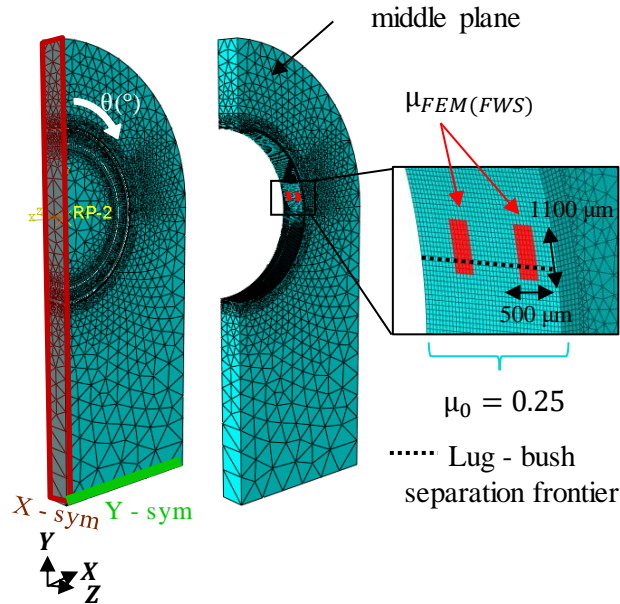


Figure 26 : Description of the Abaqus model with the fretting wear spots

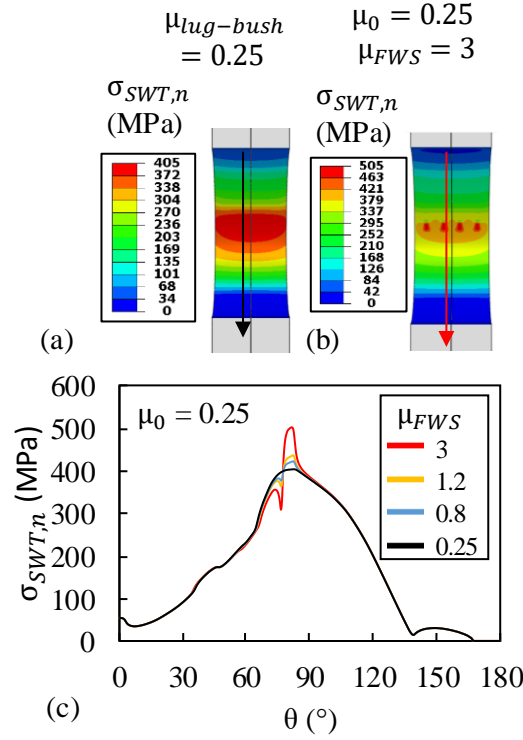


Figure 27 : (a) Distribution of SWT equivalent stress for a homogeneous coefficient of friction $\mu_0 = 0.25$ and (b) for a heterogeneous friction coefficient with $\mu_{FEM(FWS)} = 3$ at the lug-bush interface; (c) distribution of the SWT equivalent stress along the vertical line at the lug bore crossing a fretting wear spot for different $\mu_{FEM(FWS)}$; Mesh size = 100 μm , $\sigma_{nom} = 200$ MPa, IT = 30 μm , C = 100 μm , $\mu_{bush-shaft} = 0.1$, $\mu_0 = 0.25$

As shown in Figure 27c, in the presence of a spot with a high friction coefficient, the maximum SWT equivalent stress increases with increasing friction coefficient ($\mu_{FEM(FWS)}$). This spot acts as a strong stress concentration. For a friction coefficient up to 3, the maximum SWT equivalent stress was increased by about 100 MPa compared to the SWT equivalent stress with a homogeneous contact interface ($\mu_0 = 0.25$). It can be observed that the increase in SWT equivalent stress is much more significant for a model with spots with high coefficient of friction (Figure 27c) than for a model with the same coefficient of friction over the entire contact interface (Figure 25). The coefficient of friction at the fretting wear spots required for the calculated maximum equivalent stress to agree with the fatigue reference data is very high ($\mu_{FWS} \sim 3$) and well above the coefficient of friction measured with variable displacement tests ($\mu_t = 0.8$, Figure 4).

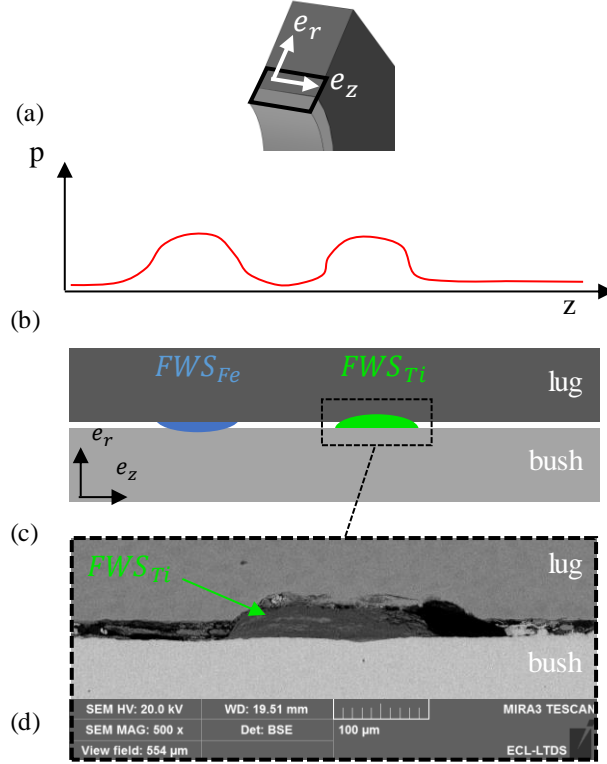


Figure 28 : (a) Illustration of the cross section of a lug-bush specimen; (b) illustration of the contact pressure distribution at the lug-bush interface due to oxide spots; (c) illustration of a lug-bush interface with oxides spots; (d) example of an observed titanium oxide spot (FWS_{Ti}) at lug-bush interface ($\sigma_{nom} = 250$ MPa, $IT = 50$ μ m, $N_{cycle} = 1.4 \times 10^5$)

However, as explained in the experimental section and illustrated in Figure 28, the fretting wear spots are likely to act as contact pressure enhancers because the lug-bush allowance at a fretting wear spot is reduced due to the increase in material volume (oxide formation). The contact pressure of the lug interface is then carried mainly by the fretting wear spots. In this context, the numerical friction coefficient at fretting spots $\mu_{FEM(FWS)}$ is a fictive coefficient of friction which takes into account both the physical coefficient of friction between wear damage rough surfaces ($\mu_t \sim 0.8$) and the local increase in shear stress due to the local increase in contact pressure induced by fretting wear spots. Considering p_{FWS} , τ_{FWS} , μ_{FWS} as the “physical” contact pressure, shear stress and friction coefficient at a fretting wear spot (for a given load), it is possible to simulate the local overpressure at the wear spot using a smooth surface by considering a fictive friction coefficient ($\mu_{FEM(FWS)}$) such as :

$$\tau_{FWS} = p_{FWS} \times \mu_{FWS} = p \times \mu_{FEM(FWS)} \quad (9)$$

with p the contact pressure for a perfectly smooth surface model. If we apply this formula, for $\mu_{FWS} = 3$ and consider that $\mu_{FWS} \sim \mu_t$, then $\frac{p_{FWS}}{p} = 3.75$, meaning that the overpressure at a fretting wear spot could be estimated to be almost four times the contact pressure considering a smooth surface.

This analysis needs further development as many hypotheses have been used. However, it does provide an explanation for the reduction in fatigue life due to fretting. Further research is needed to study the effect of the

distribution of the wear spots (size, position, number) and to improve their numerical simulation. Incremental evolution of the contact interface (such as variation of the coefficient of friction [16][52]) and stochastic modelling of the activation of the fretting wear spots would be interesting developments.

Conclusion:

Lug-bush fatigue tests were carried out to investigate the fretting fatigue behaviour of a Ti-6Al-4V (lug) - Maraging 250 (bush) assembly. The relative movements of fretting between the lug and bush induce the formation of oxides (called fretting wear spots) at the contact interface and a correlation is observed between fretting wear spot locations and crack initiation sites revealing a possible catalytic effect of wear surface damage on crack initiation.

Experimental tests show an increase in fatigue life with the interference fit which is attributed to a decrease in both stress concentration and mean stress with the interference fit level. The SWT fatigue criterion ($\sigma_{SWT,n}$) makes it possible to describe the location of the main cracking sites and to group the test points (corresponding to different levels of interference) on a single master curve. The calculated SWT equivalent stresses, especially for high numbers of cycles, are low in comparison with the reference Ti-6Al-4V fatigue behaviour. Part of the reduction in fatigue life is assumed to be due to fretting.

An increase in the coefficient of friction at the lug-bush interface cannot explain the discrepancy between the fatigue life of the tested specimens (estimated using the SWT criterion) and the material fatigue data. A numerical model with a heterogeneous coefficient of friction, which represents the fretting wear spots as areas with high coefficient of friction at the lug-bush interface, can increase the equivalent stress so as to reach the stress of the reference fatigue data.

The fatigue behaviour of pin-lug and lug-bush interfaces has been extensively studied by several researchers. Similarities and differences between these studies and the present results have been highlighted. It should be noted that the stress, strain and relative sliding distributions at the lug-bush interface are highly dependent on the geometric parameters, stiffness of the parts and interference or clearance fits between these parts. The case studied corresponds to that of a thin bush with a non-negligible bush-shaft clearance.

In order to quantify the reduction in fatigue life due to fretting alone, it will be necessary to better characterise the fatigue behaviour of the Ti-6Al-4V alloy used in order to quantify both the size effect and the notch effect on the lug-bush specimens.

Acknowledgements

The authors would like to thank Clément DEFAISSE for his help and valuable suggestions.

Bibliography:

- [1] L. Hui, H. Wang, Y. Huang, W. Yang, and S. Zhou, "Effects of different structural parameters on the 7075-T651 aluminium alloy lug structure fatigue life," *Proc. Inst. Mech. Eng. Part G J. Aerosp. Eng.*, p. 09544100221083354, 2022.
- [2] A. Strozzi, A. Baldini, and M. Nascimbeni, "Maximum equivalent stress in a pin-loaded lug subject to inclined loading," *J. Strain Anal. Eng. Des.*, vol. 41, no. 4, pp. 297–309, 2006, doi: 10.1243/03093247JSA150.
- [3] A. Strozzi, A. Baldini, M. Giacomini, E. Bertocchi, and L. Bertocchi, "Maximum equivalent stress in a pin-loaded lug in the presence of initial clearance," *J. Strain Anal. Eng. Des.*, vol. 46, no. 8, pp. 760–771, 2011, doi: 10.1177/0309324711423587.
- [4] W. D. Pilkey, D. F. Pilkey, and Z. Bi, *Peterson's stress concentration factors*. John Wiley & Sons, 2020.
- [5] J. Schijve and A. H. W. Hoeymakers, "Fatigue crack growth in lugs," *Fatigue Fract. Eng. Mater. Struct.*, vol. 1, no. 2, pp. 185–201, 1979, doi: 10.31399/asm.hb.v19.a0002360.
- [6] H. Gu *et al.*, "Crack behavior of Ti-6Al-4V alloy combined conformal contact fretting , non- conformal contact fretting and simple fatigue," *Int. J. Fatigue*, vol. 139, no. May, p. 105741, 2020, doi: 10.1016/j.ijfatigue.2020.105741.
- [7] W. A. P. Fisher and W. J. Winkworth, "Improvements in the fatigue strength of joints by the use of interference fits," *Aeronaut. Res. Counc. reports Memo.*, vol. 2874, 1952.
- [8] A. Buch, "Fatigue and fretting of pin-lug joints with and without interference fit," *Wear*, vol. 43, no. 1, pp. 9–16, 1977.
- [9] J. Ransom, D. J. Reddy, T. Poast, and E. Rejzek, "Fatigue strength improvement of helicopter lugs with the ForceMate process : analytical prediction versus test results," *Proceedings, Annu. Forum Am. Helicopter Soc.*, vol. 64, no. 3, pp. 2147–2155, 2008.
- [10] M. A. Brown and J. L. Evans, "Fatigue life variability due to variations in interference fit of steel bushings in 7075-T651 aluminum lugs," *Int. J. Fatigue*, vol. 44, pp. 177–187, 2012, doi: 10.1016/j.ijfatigue.2012.05.001.
- [11] R. Amargier, "Amorçage de fissures et gradient de contrainte en fretting et en fatigue," 2011.
- [12] R. Wardlaw, M. Shultz, and D. J. Reddy, "Fatigue strength improvement of helicopter steel and titanium lugs with the ForceMate process: analytical prediction versus test results," *Am. helicopter Soc. 67th Annu. forum, Virginia beach, Virginia*, no. 6, pp. 2643–2649, 2011.
- [13] T. N. Chakherlou, H. Taghizadeh, and A. B. Aghdam, "Experimental and numerical comparison of cold expansion and interference fit methods in improving fatigue life of holed plate in double shear lap joints," *Aerosp. Sci. Technol.*, vol. 29, no. 1, pp. 351–362, 2013, doi: 10.1016/j.ast.2013.04.006.

- [14] E. B. Ozen, Y. M. Korkmaz, and D. Coker, "Investigation of fretting fatigue failure mechanism of lug-bush connection members," in *Procedia Structural Integrity*, 2019, vol. 21, pp. 215–223, doi: 10.1016/j.prostr.2019.12.104.
- [15] N. Antoni, "A study of contact non-linearities in pin-loaded lugs: Separation, clearance and frictional slipping effects," *Int. J. Non. Linear. Mech.*, vol. 58, pp. 258–282, 2014, doi: 10.1016/j.ijnonlinmec.2013.09.007.
- [16] A. Mäntylä, J. Hintikka, T. Frondelius, J. Vaara, A. Lehtovaara, and J. Juoksukangas, "Prediction of contact condition and surface damage by simulating variable friction coefficient and wear," *Tribol. Int.*, vol. 143, no. October 2019, 2020, doi: 10.1016/j.triboint.2019.106054.
- [17] H. Gu, L. Jiao, P. Yan, B. Ma, S. Chen, and L. Feng, "Crack behavior of Ti-6Al-4V alloy combined conformal contact fretting, non-conformal contact fretting and simple fatigue," *Int. J. Fatigue*, vol. 139, pp. 1–19, 2020, doi: 10.1016/j.ijfatigue.2020.105741.
- [18] B. Badding, M. Bhalerao, J. P. Dowell, R. Gambheera, and S. Sundaram, "A Method to Predict Fretting in Diesel Engine Connecting Rod Bearing Bores," *Intern. Combust. Engine Div. Fall Tech. Conf.*, vol. 37467, pp. 607–616, 2004.
- [19] A. Strozzi, A. Baldini, M. Giacomini, E. Bertocchi, and S. Mantovani, "A repertoire of failures in connecting rods for internal combustion engines , and indications on traditional and advanced design methods," *Eng. Fail. Anal.*, vol. 60, pp. 20–39, 2016, doi: 10.1016/j.engfailanal.2015.11.034.
- [20] J. Juoksukangas *et al.*, "Characterization of cracks formed in large flat-on-flat fretting contact," *Int. J. Fatigue*, vol. 124, no. December 2018, pp. 361–370, 2019, doi: 10.1016/j.ijfatigue.2019.03.004.
- [21] Y. Huang, H. Li, X. Yang, Z. Guan, Z. Li, and Y. Sun, "Improving the fatigue life of 2297-T87 aluminum-lithium alloy lugs by cold expansion, interference fitting, and their combination," *J. Mater. Process. Technol.*, vol. 249, no. June, pp. 67–77, 2017, doi: 10.1016/j.jmatprotec.2017.06.004.
- [22] C. Ruiz, P. Boddington, and K. C. Chen, "An investigation of fatigue and fretting in a dovetail joint," *Exp. Mech.*, vol. 24, no. 3, pp. 208–217, 1984, doi: 10.1007/BF02323167.
- [23] D. Merritt and G. Zhu, "The prediction of connecting rod fretting and fretting initiated fatigue fracture," *SAE Tech. Pap.*, vol. 2004, no. 724, 2004, doi: 10.4271/2004-01-3015.
- [24] C. Jiménez-Peña, R. H. Talemi, B. Rossi, and D. Debruyne, "Investigations on the fretting fatigue failure mechanism of bolted joints in high strength steel subjected to different levels of pre-tension," *Tribol. Int.*, vol. 108, no. November 2016, pp. 128–140, 2017, doi: 10.1016/j.triboint.2016.11.014.
- [25] J. F. W. Leung, R. Voothaluru, and R. W. Neu, "Predicting white etching matter formation in bearing steels using a fretting damage parameter," *Tribol. Int.*, vol. 159, no. February, p. 106966, 2021, doi: 10.1016/j.triboint.2021.106966.
- [26] J. Ding, W. S. Sum, R. Sabesan, S. B. Leen, I. R. McColl, and E. J. Williams, "Fretting fatigue predictions in a complex coupling," *Int. J. Fatigue*, vol. 29, no. 7, pp. 1229–1244, 2007, doi:

- 10.1016/j.ijfatigue.2006.10.017.
- [27] D. Mangardich, F. Abrari, and Z. Fawaz, "A fracture mechanics based approach for the fretting fatigue of aircraft engine fan dovetail attachments," *Int. J. Fatigue*, vol. 129, no. July, p. 105213, 2019, doi: 10.1016/j.ijfatigue.2019.105213.
 - [28] J. A. Hines and G. Lütjering, "Propagation of microcracks at stress amplitudes below the conventional fatigue limit in Ti-6Al-4V," *Fatigue Fract. Eng. Mater. Struct.*, vol. 22, no. 8, pp. 657–665, 1999, doi: 10.1046/j.1460-2695.1999.00217.x.
 - [29] S. Fouvry, P. Duó, and P. Perruchaut, "A quantitative approach of Ti-6Al-4V fretting damage: Friction, wear and crack nucleation," *Wear*, vol. 257, no. 9–10, pp. 916–929, 2004, doi: 10.1016/j.wear.2004.05.011.
 - [30] H. Proudhon, S. Fouvry, and J. Y. Buffière, "A fretting crack initiation prediction taking into account the surface roughness and the crack nucleation process volume," *Int. J. Fatigue*, vol. 27, no. 5, pp. 569–579, 2005, doi: 10.1016/j.ijfatigue.2004.09.001.
 - [31] Z. Y. Li, X. L. Liu, G. Q. Wu, and Z. Huang, "Fretting Fatigue Behavior of Ti-6Al-4V and Ti-10V-2Fe-3Al Alloys," *Met. Mater. Int.*, vol. 25, no. 1, pp. 64–70, 2019, doi: 10.1007/s12540-018-0158-8.
 - [32] D. Knabner, S. Hauschild, L. Suchý, S. Vetter, and A. Hasse, "Calculation method for the fail-safe design of steel – steel contacts subject to fretting fatigue based on a worst-case assumption," *Int. J. Fatigue*, p. 107217, 2022, doi: 10.1016/j.ijfatigue.2022.107217.
 - [33] R. Lewis, M. B. Marshall, and R. S. Dwyer-Joyce, "Ultrasonic characterisation of an interference fit," *Tribol. Ser.*, vol. 41, no. 1, pp. 449–458, 2003.
 - [34] R. Lewis, M. B. Marshall, and R. S. Dwyer-Joyce, "Measurement of interface pressure in interference fits," *Proc. Inst. Mech. Eng. Part C J. Mech. Eng. Sci.*, vol. 219, no. 2, pp. 127–139, 2005, doi: 10.1243/095440605X8432.
 - [35] E. B. Özen, "Experimental and numerical investigation of fretting failure in lug-bush members under cyclic loading," 2021.
 - [36] C. Cherpin, D. Lister, F. Dacquait, and L. Liu, "Study of the Solid-State Synthesis of Nickel Ferrite (NiFe₂O₄) by X-ray Diffraction (XRD), Scanning Electron Microscopy (SEM) and Raman Spectroscopy," pp. 0–9, 2021.
 - [37] W. Tian and T. Q. Zhu, "Supporting Information of Raman study of Yuan Qinghua porcelain : The highlighting of dendritic CoFe₂O₄ crystals in blue decorations Raman study of Yuan Qinghua porcelain : the highlighting of dendritic CoFe₂O₄ crystals in blue decorations," no. October, pp. 2–5, 2016.
 - [38] P. B. Kharat, S. B. Somvanshi, J. S. Kounsalye, S. S. Deshmukh, P. P. Khirade, and K. M. Jadhav, "Temperature dependent viscosity of cobalt ferrite / ethylene glycol ferrofluids," *AIP Conf. Proc.*, vol. 1942, pp. 1–5, 2018, doi: 10.1063/1.5028675.

- [39] J. J. Arnoux, G. Sutter, G. List, P. Bourson, and H. Chaynes, "Raman characterization of Ti-6Al-4V oxides and thermal history after kinetic friction," *Phase Transitions*, vol. 87, no. 6, pp. 559–570, 2014, doi: 10.1080/01411594.2013.871720.
- [40] C. H. Hager, J. H. Sanders, and S. Sharma, "Characterization of mixed and gross slip fretting wear regimes in Ti6Al4V interfaces at room temperature," *Wear*, vol. 257, no. 1–2, pp. 167–180, 2004, doi: 10.1016/j.wear.2003.10.023.
- [41] J. P. Gallagher, R. H. van Stone, R. E. DeLaneuville, P. Gravett, and R. S. Bellows, "Improved high-cycle fatigue (HCF) life prediction," 2001.
- [42] A. K. Rao, "Elastic analysis of pin joints," *Comput. Struct.*, vol. 9, no. 2, pp. 125–144, 1978, doi: 10.1016/0045-7949(78)90131-1.
- [43] C. Paulin, S. Fouvry, and C. Meunier, "Finite element modelling of fretting wear surface evolution: Application to a Ti-6Al-4V contact," *Wear*, vol. 264, no. 1–2, pp. 26–36, 2008, doi: 10.1016/j.wear.2007.01.037.
- [44] B. Boddington, K. Chen, and C. Ruiz, "The numerical analysis of dovetail joints," *Comput. Struct.*, vol. 20, no. 4, pp. 731–735, 1984.
- [45] M. P. Szolwinski and T. N. Farris, "Mechanics of fretting fatigue crack formation," *Wear*, vol. 198, no. 1–2, pp. 93–107, 1996, doi: 10.1016/0043-1648(96)06937-2.
- [46] G. Q. Wu, C. L. Shi, W. Sha, A. X. Sha, and H. R. Jiang, "Effect of microstructure on the fatigue properties of Ti-6Al-4V titanium alloys," *Mater. Des.*, vol. 46, pp. 668–674, 2013, doi: 10.1016/j.matdes.2012.10.059.
- [47] J. Bellecave, "Stress Gradients In Fretting Fatigue," 2015.
- [48] J. Schijve, "Contribution to the theory of aircraft structures," in *Contributions to the theory of aircraft structures*, 1972, pp. 423–440.
- [49] J. Schijve, D. Broek, and F. A. Jacobs, *Fatigue tests on aluminium alloy lugs with special reference to fretting*. NLR-TN M., 1962.
- [50] D. J. White, "The fatigue strength of large single-pinned and double-pinned connections made from alloy steel FV520B," *Proc. Inst. Mech. Eng.*, vol. 1, pp. 563–578, 1968.
- [51] S. E. Larsson, "The development of a calculation method for the fatigue strength of lugs and a study of test results for lugs of aluminium," *Fatigue Des. Proced.*, pp. 309–342, 1969, doi: 10.1016/b978-0-08-011697-6.50017-5.
- [52] T. Yue and M. Abdel Wahab, "Finite element analysis of fretting wear under variable coefficient of friction and different contact regimes," *Tribol. Int.*, vol. 107, no. November 2016, pp. 274–282, 2017, doi: 10.1016/j.triboint.2016.11.044.